REGENERATION

Injury-induced electrochemical coupling triggers organ growth

Jinghui Liu[1,2,3,4]†, Elisa Nerli[1,2]†, Charlie Duclut[5]‡, Amit S. Vishen[3]‡§, Naomi Berbee[1,2], Sylvia Kaufmann[1,2], Cesar Ponce[1,2], Aristides B. Arrenberg[6]¶, Frank Jülicher[2,3,4]*, Rita Mateus[1,2]*

Organ injury triggers nonneuronal electric currents essential for regeneration. However, the mechanisms by which electrical signals are generated, sensed, and transmitted upon damage to promote organ growth remain unclear. Here, we uncover that organ repair relies on dynamic electrochemical coupling between membrane potential depolarization and intracellular signaling, essential to activate cell proliferation. By subsecond live imaging of locally injured zebrafish larval fins, we identify events across time and space: a millisecond, long-range, membrane depolarization gradient, followed by second-persistent intracellular calcium responses. In the subsequent hour, voltage sensing phosphatase senses the injury-driven membrane potential change and autonomously translates the electric signal intracellularly, promoting tissue-wide cell proliferation. Connecting these dynamics with an electrodiffusive model showed that ionic fluxes and electric potential become coupled in the fin's interstitial space, enabling organ-wide signal spreading. Our work reveals the coupling between fast electrical signals and slower intracellular signaling, ensuring complete organ recovery.

INTRODUCTION

Membrane potential (V_{mem}) is a ubiquitous and essential property of all cells, established by ionic fluxes across membranes (*1*). While modulation of V_{mem} has been shown to have a direct impact in developmental and regenerative processes (*2*–*9*), how these signals instruct specific cellular behaviors is still scarcely understood.

In epithelia and epithelia-lined organs, individual cellular V_{mem} assumes a collective, nonautonomous behavior, the transepithelial potential (*10*, *11*). On one hand, this effect stems from the polarized distribution of ion pumps in apical versus basolateral epithelial cell membranes, generating asymmetries in ion fluxes (*12*–*14*). On the other hand, epithelial tissue layers can be electrically coupled by the presence of gap junctions, which allow for rapid intercellular ion transport (*15*, *16*). Furthermore, epithelial sheets are often protective barriers (*17*), a function that requires the presence of high-resistance tight junctions between cells (*18*), contributing to the transepithelial potential difference between the inside and outside of organs (*19*).

Upon organ injury, a prevalent aspect of multicellular life, the protective barrier is breached because of tight junction disruption, causing lower resistance in the tissue, short-circuiting the organ's transepithelial potential (*20*–*22*). This results in collective ion leakage, generating an organ-outward wound current (*21*, *23*–*25*) with magnitudes between 50 and 500 mV/mm (*26*, *27*), which is essential for functional organ healing across species (*28*–*30*), and can be long lasting for hours (*31*). However, it remains elusive how cell-based ionic flows work as an injury-sensing mechanism and, collectively, lead to tissue-scale electric fields necessary for organ repair and regeneration.

Beyond wound currents, tissue damage is also known to induce a set of transcription-independent early injury responses (*32*), many conserved across species (*33*–*43*). Despite having different spatiotemporal dynamics, these signals convey damage recognition and relay of such information throughout the tissue, activating downstream repair processes (*30*, *34*, *36*–*39*, *41*). In regeneration-competent organs, the early injury responses are also linked to initiation of specific transcriptional programs resulting in activation of cellular sources, enabling restoration of organ architecture and functionality (*33*, *44*, *45*). At the heart of such successful restoration is the kickstart of cell proliferation in injured tissues (*45*).

Across fish species, perturbing ion flux invariably affects fin size (*25*, *46*–*54*), suggesting a role for electrical signals in controlling processes such as cell proliferation and tissue growth. However, how V_{mem} changes can regulate proliferation during organ development and regeneration remains unknown. We therefore asked how does organ damage affect tissue-scale bioelectrical states? How are electrical signals spatiotemporally generated in tissues and sensed by cells to promote organ (regenerative) growth?

Here, we applied ultraviolet (UV)–laser microdissection to precisely injure zebrafish larval fins while live imaging cellular responses with subsecond resolution. This allowed us to quantitatively map the spatiotemporal dynamics of V_{mem} and calcium (Ca^{2+}) signals in vivo. We found that organ injury leads to an immediate tissue-scale membrane depolarization gradient, followed by a diffusive Ca^{2+} wave. To understand the onset and propagation of these signals at milli- to second timescales in the finfold, we developed electrodiffusive theory, coupling ion fluxes to tissue-scale V_{mem} and Ca^{2+} dynamics. This clarified that the spreading and persistence of these signals in the injured organ are rooted in ionic diffusion, providing a physical cause for the initiation and propagation of wound currents and postinjury intracellular Ca^{2+} signaling in tissues.

[1]Max Planck Institute of Molecular Cell Biology and Genetics, 01307 Dresden, Germany. [2]Cluster of Excellence Physics of Life, Technische Universität Dresden, 01062 Dresden, Germany. [3]Max Planck Institute for the Physics of Complex Systems, 01187 Dresden, Germany. [4]Center for Systems Biology Dresden, 01307 Dresden, Germany. [5]Laboratoire Physique des Cellules et Cancer, CNRS UMR 168, Institut Curie, Université PSL, Sorbonne Université, 75005 Paris, France. [6]Centre for Biological Signalling Studies (BIOSS), Developmental Biology 1, Faculty of Biology, Albert-Ludwigs-University Freiburg, 79104 Freiburg, Germany.
*Corresponding author. Email: julicher@pks.mpg.de (F.J.); mateus@mpi-cbg.de (R.M.)
†These authors contributed equally to this work.
‡These authors contributed equally to this work.
§Present address: Centre for Mechanochemical Cell Biology and Division of Biomedical Sciences, Warwick Medical School, University of Warwick, Coventry CV4 7AL, UK.
¶Present address: Werner Reichardt Centre for Integrative Neuroscience, Institute of Neurobiology, University of Tübingen, 72076 Tübingen, Germany.

Manipulating V_{mem} and the ionic composition of the larval fin's interstitial fluid (IF) proved sufficient to not only alter the spatiotemporal dynamics of injury-induced Ca^{2+} signaling but also modulate tissue-wide cell proliferation and subsequent organ regrowth. Unexpectedly, we found that V_{mem} depolarization prompts cell proliferation within 1 hour postinjury, this being essential for successful finfold repair and regrowth 3 days after.

At the molecular level, we identified that the injury-induced V_{mem}-depolarizing signal is sensed and transduced by a conserved transmembrane protein, voltage sensing phosphatase (VSP). Cell autonomous VSP activity through lipid dephosphorylation at the membrane is necessary and sufficient to trigger the cell proliferation observed at 1 hour postinjury, enabling complete organ repair. Last, in the absence of damage, we show that stimulating VSP activity leads to longer finfolds, supporting a role for tissue-wide electrical signals as a potential general mechanism contributing to organ size. Our findings uncover a bioelectric injury-sensing mechanism that conveys ultrafast cell-to-cell communication, necessary to initiate organ regrowth.

RESULTS

A tissue-scale membrane depolarization gradient precedes a Ca^{2+} wavefront upon organ injury

To investigate the spatiotemporal dynamics of electrical signals elicited by organ damage, we established an in vivo live imaging assay joining optical electrophysiology tools with precise UV-laser microdissection. This allowed millisecond resolution of tissue-scale signal dynamics induced by injury in the 2–days postfertilization zebrafish larval caudal finfold (Materials and Methods).

The 2-days postfertilization larval fin exhibits simple planar tissue architecture, consisting of two adjacent epithelial layers that enclose fibroblast-like cells and structural elements within its IF (Fig. 1A and fig. S1C). The presence of tight junctions in the apical epithelial layer of the finfold makes this tissue an effective barrier to the extraembryonic environment (*55*, *56*), guaranteeing high electrical resistance (Fig. 1, A′ and B, and fig. S1A) (*18*). Notably, we find that gap junctions are also restricted to this finfold layer (Fig. 1, A′ and B, and fig. S1B), providing electrical coupling (i.e., similar V_{mem}) among apical epithelial cells (*15*, *16*).

We first focused on quantifying the postinjury dynamics of intracellular Ca^{2+}, given previous reports that it composes one of the earliest wound signals that can direct cellular responses (*30*, *33*–*38*, *43*). Applying our live imaging assay, we detected the formation of a tissue-scale Ca^{2+} wavefront as early as 100 ms postinjury, initiated by wound-adjacent cells (Fig. 1C, fig. S2A, and movie S1). By combining Ca^{2+} signaling transgenics [Tg(ubb:GCaMP6f)^{m1299}, i.e., ubb:GCaMP6f] with epithelial membrane reporter lines [apical epithelial layer: Tg(−8.0cldnb:lynGFP)^{zf106}, i.e., claudinb:Lyn-GFP; basal epithelial layer: Tg(tp63:CAAX-GFP)^{mdi2013Tg}, i.e., tp63:CAAX-GFP], we found that this wavefront concomitantly propagates in both epithelial finfold layers up to ~120 μm from the wound (apical: 118.4 ± 14.3 μm, basal: 118.7 ± 8.5 μm), slowing down and stopping at ~5 s after injury (apical: 4.9 ± 0.9 s, basal: 5.3 ± 1.0 s) (Fig. 1D and movie S1). At 15 s after injury, only wound-adjacent cells showed elevated Ca^{2+} levels. In the subsequent 30s, Ca^{2+} flashes occur in single epithelial cells traversed by the wavefront (movie S1).

To understand the basis of the Ca^{2+} wavefront activation, we measured the total intracellular Ca^{2+} intensity change per cell (Fig. 1E and fig. S2B) and extracted a characteristic time of Ca^{2+} cell activation (Materials and Methods). We found a robust power-law dependence between distance from wound and Ca^{2+} activation time, with a ~0.5 exponent in both finfold epithelial layers (apical cells: 0.48 ± 0.02, basal cells: 0.46 ± 0.01; Fig. 1F and fig. S2, C and D), indicating diffusive (*57*) propagation of the Ca^{2+} activation signal from the injury. We then extracted diffusion coefficients per layer (apical: 1677 ± 170 μm^2/s, basal: 1877 ± 179 μm^2/s; Fig. 1F and fig. S2, C and D), which are in comparable ranges to ion diffusivity in aqueous medium [Na^+: 1334 μm^2/s, K^+: 1957 μm^2/s, and Cl^-: 2032 μm^2/s (*58*)]. Notably, this diffusive propagation is invariant to differences in injury shape, size (fig. S3, A and B, and movie S2), or type (laser or mechanical cut; fig. S3C and movie S3). Furthermore, analyzing the Ca^{2+} wave dynamics in transgenics expressing only ubb:GCaMP6f ensured that these dynamics were not obscured by membrane green fluorescent protein (GFP) signals (figs. S2C versus S12H and movies S10 and S11).

The subsecond Ca^{2+} wavefront dynamics occurring in both finfold epithelial layers suggested the presence of a signal that could act faster than known chemical regulators arising upon injury (*32*). In particular, the observed diffusive Ca^{2+} dynamics pointed toward a physical mechanism rooted in tissue-scale ion fluxes altered by organ injury, i.e., a wound current (*21*, *23*–*25*).

Motivated by the known coupling between Ca^{2+} signaling and voltage changes in single cells, namely, neurons (*59*, *60*), we asked how the injury affects V_{mem}. To probe changes in V_{mem} per epithelial layer, we expressed a fluorescence resonance energy transfer (FRET)-based voltage reporter, Voltron2 (*61*), into the previously used apical or basal epithelial membrane reporter lines (Fig. 1, G and H; fig. S4, A- and B; and Materials and Methods) and applied our live imaging injury assay.

Notably, at 100 ms after injury, we detected widespread membrane depolarization in cells of both epithelial finfold layers, corresponding to a spatially graded drop of Voltron2 fluorescence spanning ~200 μm from the wound (Fig. 1, H, I, and K, and fig. S4, A and B). In contrast, at 100 ms, intracellular Ca^{2+} is only activated within 20 μm from the wound (Fig. 1C). Over the next 5 s, Voltron2 intensity is maintained (Fig. 1J), suggesting that cells remain depolarized, as the Ca^{2+} wavefront propagates through the finfold. By quantifying the fractional change of Voltron2 intensity occurring after cut ($-\Delta F/F_{uncut}$; Materials and Methods), we found that the spatial gradient of V_{mem} depolarization displays an exponential profile with comparable characteristic lengths l for both epithelial layers (apical: 206 ± 48 μm, basal: 187 ± 24 μm; Fig. 1K and fig. S4, C to F). These results establish that a tissue-scale depolarization gradient spatiotemporally precedes the Ca^{2+} wave in injured larval fins, and together, these multiscale signals compose the earliest tissue-wide injury responses yet detected.

Multicompartment electrodiffusion model explains voltage and Ca^{2+} injury responses

Our measurements of the larval fin injury responses led to two central questions: How does a local lesion induce a widespread (~200 μm) membrane potential response in a tissue within milliseconds (100 ms)? How do Ca^{2+} injury responses emerge on a different timescale than voltage yet displaying activation dynamics similar to ionic diffusion? To address these, we developed electrodiffusion theory in multiple compartments to solve for the changes of ion fluxes and electric potentials upon injury in the 2-days postfertilization larval

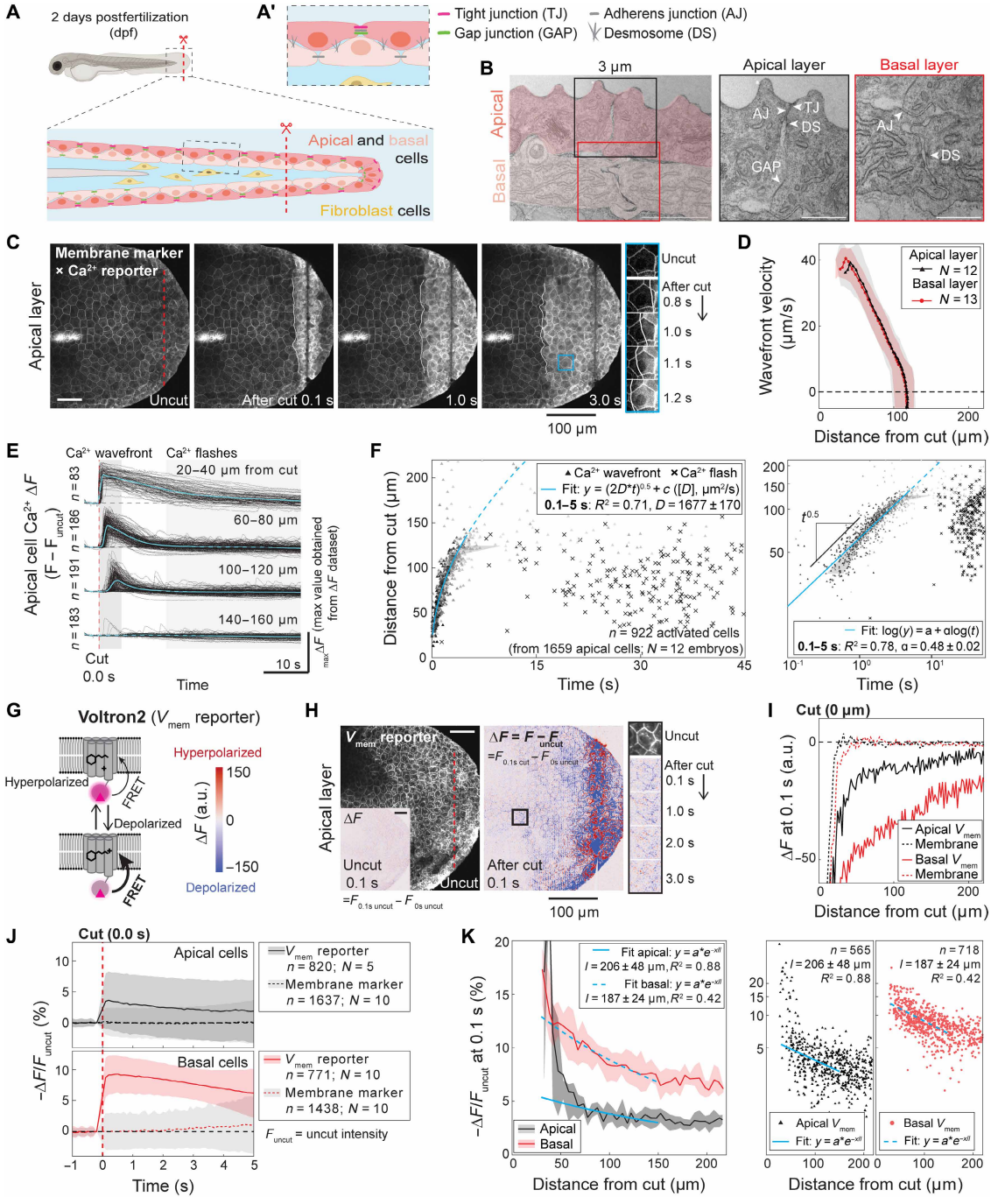

Fig. 1. A membrane depolarization gradient and diffusive Ca^{2+} wavefront are rapid organ-wide injury responses. (**A**) Zebrafish larva at 2 days postfertilization (dpf), highlighting caudal finfold architecture, junctions (A′), and amputated region (red dash). (**B**) Micrographs of 2-days postfertilization finfold with annotated junctions in apical (black) and basal (red) epithelial layers. (**C**) Two-days postfertilization finfold before and after cut in transgenics labeling intracellular Ca^{2+} (ubb:GCaMP6f) and membranes of apical epithelial cells (claudinb:Lyn-GFP). Blue inset: Cellular detail. White lines: Ca^{2+} wavefront. (**D**) Velocity of Ca^{2+} wavefront versus position relative to wound in apical (black) and basal (red) epithelia. Shades: SD. (**E**) Change of cytosolic Ca^{2+} intensity (ΔF) versus time. Cyan: average. (**F**) Position of apical cells relative to wound versus time of Ca^{2+} wavefront (triangle) or flash (cross) activation. Shade: 25 to 75% percentile. Cyan lines: diffusive fit in linear scale (D: diffusion coefficient), linear fit in log-to-log scale (right) (α: scaling exponent) (0.1 to 5 s). Cyan dash: diffusive fit at 0.1 to 20 s. (**G**) Voltron2 schematics. a.u., arbitrary units. (**H**) Left: Apical epithelium of uncut 2-days postfertilization finfold labeled with Voltron2. Inset: Change of Voltron2 intensity (ΔF) in uncut. Right: Change of Voltron2 intensity (ΔF) at 0.1 s postcut. Black inset: Cellular detail. (**I**) At 0.1 s postcut, changes of Voltron2 (line) or membrane fluorescence (dash) intensity (ΔF) versus position relative to wound, per epithelial layer. (**J**) Average fractional drop of Voltron2 or membrane fluorescence intensity per cell over time ($-\Delta F/F_{uncut}$). Shades: SD. (**K**) At 0.1 s postcut, fractional drops of Voltron2 intensity ($-\Delta F/F_{uncut}$) in apical or basal cells versus position relative to wound. Left: Mean and 25 to 75% percentiles. Right: Individual apical or basal cells. Cyan: exponential fits in linear (left) and log-to-linear (right) scales. Error: 95% confidence interval (CI) of parameter fits. R^2: goodness of fit. N: number of larvae [(D), (F), (I), and (J)]. n: number of cells [(E), (F), (J), and (K)]. Scale bars, 50 µm [(C) and (H)], 2 µm, and 1 µm (B).

fin. Our theory minimally describes this organ as an electrically coupled epithelial sheet that separates the high-osmolarity IF (*62*, *63*) from the low-osmolarity extraembryonic environment (Fig. 2A). The inherent leakiness of the tight junctions present in the finfold's apical epithelial layer at this developmental stage (*55*) allows for paracellular ion fluxes (*19*) between the interstitial and extraembryonic spaces (Fig. 2A and note S1).

The injury leads to a sudden change of tissue boundaries: the high and low osmolarity media from inside and outside the zebrafish become connected (Fig. 2A′), inducing the short circuit of the finfold's transepithelial potential (*20*–*22*). This short circuit corresponds to changes of individual cellular V_{mem} that are spatiotemporally coupled in the tissue via electrodiffusive dynamics of cation (Na^+) and anion (Cl^-) species inside the finfold's interstitial space (Fig. 2B and note S1). Our model postulates that, upon injury, the electric potential and ion concentration change at different timescales.

The first response, occurring at milliseconds, pertains to the electric potential and is faster than ion diffusion (*58*). Hence, the dynamics of electric potential reduces to that of cable theory (*64*, *65*). Here, cable theory represents the epithelium as a capacitor and resistor in parallel, taking into account the conductivity of the IF (Fig. 2B and note S2). Upon injury, the electric potential in the IF relaxes to a quasi–steady state over 100 ms. After relaxation, it assumes an exponential profile that decays over a characteristic length $l = \sqrt{D/\Lambda}$, set by the diffusion constant of ions D, and the parameter Λ, describing ion leakage through tight junctions. By explicitly considering ion transport across the basolateral cell membrane facing the IF, we show that the potential difference across this membrane is proportional to the transepithelial potential and therefore also assumes an exponential profile (Fig. 2B, top graph). Using diffusion constants of Na^+ and Cl^-, geometric parameters from the finfold architecture (fig. S1, D and E) and the determined characteristic length l (Fig. 1K), we estimate the epithelial ion permeability to be $\Lambda = 0.05\ s^{-1}$ (note S3). For typical concentration of ions in the zebrafish IF (*62*, *63*), this corresponds to an epithelium resistance in unit area of ~200 ohm·cm^2, well within the range of values reported for resistance of epithelial tissues (*18*).

At a slower timescale, seconds subsequent to injury, ion diffusion takes place from the highly concentrated IF to the low-concentration extraembryonic medium. Here, the dynamics of ions and electric potential become coupled, being well described by effective diffusion equations with a source term stemming from ion transport across the larval fin's apical epithelium (Fig. 2B and note S2). As a result, an ionic concentration profile is established along the larval fin's interstitial space from the wound site (Fig. 2B, bottom graph). This spatial concentration profile is predicted to drive the postwound intracellular Ca^{2+} dynamics, leading to the observed diffusive activation wave in the tissue.

To test whether the observed Ca^{2+} wave could originate from sources alternative to our model's proposed explanation, we performed injury experiments, depleting the extraembryonic Ca^{2+} in the media and blocking gap-junction pore formation. The postinjury Ca^{2+} wave dynamics remained unaffected in both situations (fig. S5 and movies S5 and S7), corroborating our model's result that the observed postinjury Ca^{2+} wave is accounted for by the ion concentration gradient dynamics established along the larval fin's IF (Fig. 2, A′ and B).

Last, to further understand the dynamics of the observed Ca^{2+} injury responses at the single-cell level, we also developed a minimal nonlinear model that qualitatively captures the rising time and amplitude decrease (Fig. 2C and note S3). This recapitulates an activation front of intracellular Ca^{2+} with a close-to-ion diffusion coefficient (Fig. 2D and movie S4). Moreover, the dispersion of the experimental Ca^{2+} activation data (Fig. 1F and fig. S2C) can be accounted for in a stochastic version of the model (fig. S18 and note S3). Together, our results put forward that the observed postinjury dynamics of Ca^{2+} signaling are driven solely by the electrical and ionic changes that take place inside the larval fin's interstitial space.

Potassium flux remodels organ-scale injury responses

Our physical model suggests that the observed Ca^{2+} wave is rooted in the ionic changes occurring in the larval fin upon injury, i.e., the wound current. We thus asked whether changing ion composition and fluxes would spatiotemporally affect this injury response. We focused on potassium (K^+) because this ion plays a central role both in setting the cellular V_{mem} (*66*) and is connected to fish fin size regulation through activity of specific channels (*47*, *49*–*52*, *54*). Considering this, we incorporated K^+ into our model (note S4), predicting that K^+ perturbations would lead to changes in the larval fin's IF ionic composition and modifying the cell's V_{mem}.

In the first prediction, considering the tight junction ion permeability in the finfold's apical epithelium and the low K^+ concentration in the finfold's interstitial space (*62*, *63*), the IF ionic composition should change upon exposure to high extraembryonic K^+, resulting in altered electrodiffusive Ca^{2+} responses upon injury (note S4). To test this, we incubated larvae in highly concentrated potassium chloride (high KCl) (Materials and Methods). By inducing injuries under this condition, the Ca^{2+} wave propagated for more than 300 μm in the finfold, threefold longer than wild type (WT) (Fig. 2, E and F; fig. S6, A, B, and B′; and movies S8 and S9). This Ca^{2+} wave also propagated with a smaller diffusion coefficient compared to WT (Fig. 2, G and H), consistent with our theory (note S4).

Second, our theory also predicts a direct effect of high KCl on the V_{mem} shared by the apical epithelial finfold cells, independently of injury (note S4). This is rooted in a reduction of the K^+'s cellular efflux (*66*), given the high extraembryonic KCl concentration. By measuring Voltron2 intensity while treating larvae with high KCl, we verified that indeed the V_{mem} of apical epithelial cells becomes depolarized (fig. S6E). This treatment also led to a reduction of wound-induced Ca^{2+} flashes in the same finfold layer (Fig. 2H, fig. S7C, and movie S9), reminiscent of neuronal systems where high KCl affects single-cell Ca^{2+} flashes (*60*, *67*).

In contrast, we rationalized that cellular K^+ efflux would be increased with two known functional assays, leading also to V_{mem} hyperpolarization (*47*, *54*, *68*–*71*): *kcnh2a*$^{lof/lof}$ gain-of-function mutants, which present ectopic up-regulated expression of *kcnh2a*, a K^+ voltage-gated channel (*51*–*53*), and FK506 treatment, a Calcineurin inhibitor known to interact with *kcnk5b* K^+ leak channels, maintaining them open (*48*, *49*, *54*). In both cases, injury led to prominent Ca^{2+} flash increase in the apical finfold epithelium (Fig. 2J; figs. S6, C and D′, and S7, C and D; and movie S9). The Ca^{2+} wave, on the other hand, remained mostly unaffected under these conditions (Fig. 2, I and J; and figs. S6, C and D′, and S7, A and B). Together, we conclude that K^+ flux modulation is sufficient to markedly remodel voltage and Ca^{2+} injury responses in space and time by regulating the larval fin's IF ionic composition and V_{mem}.

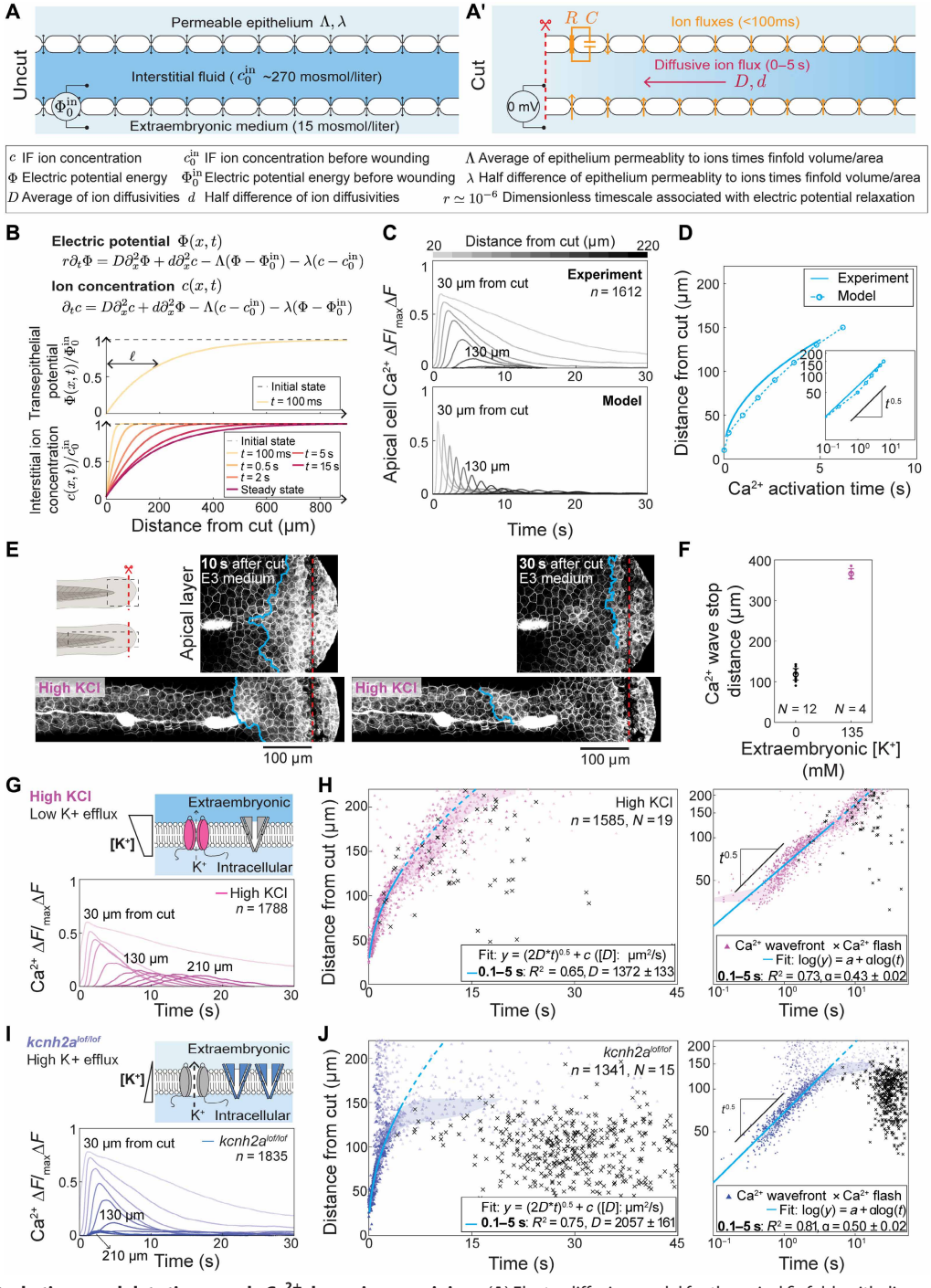

Fig. 2. Potassium perturbations modulate tissue-scale Ca^{2+} dynamics upon injury. (**A**) Electrodiffusive model for the apical finfold epithelium enclosing IF, before and after cut (A′). (**B**) Top: Predicted changes of transepithelial potential versus position relative to wound within 100 ms. Bottom: Predicted changes of IF ionic concentration versus position relative to wound between 100 ms and 15 s, with steady-state profile. Model equations obtained using electroneutral approximation of Poisson-Nernst equations for two monovalent ionic species. See box for symbolic representations. (**C**) Top: Measurements of position-averaged changes of normalized cytosolic Ca^{2+} intensity ($\Delta F/_{max}\Delta F$, $_{max}\Delta F$ = max value obtained from ΔF dataset, normalized per embryo) versus time. Bottom: Model calculated changes of the cytosolic Ca^{2+} versus time. (**D**) Diffusive fit to Ca^{2+} front position versus time in experiments (line; from Fig. 1F) versus model (dash). (**E**) Two-days postfertilization fins at 10 s (left) and 30 s (right) after cut in transgenics labeling intracellular Ca^{2+} (ubb:GCaMP6f) and apical epithelial membranes (claudinb:Lyn-GFP) in E3 medium (top) or KCl-treated (bottom) conditions. Cyan: Ca^{2+} wavefront. (**F**) Ca^{2+} front traverse distance in control (5 s) versus in KCl-treated larvae (45 s). Error bars: SD. (**G** and **I**) Position-averaged changes of normalized cytosolic Ca^{2+} intensity ($\Delta F/_{max}\Delta F$) from apical epithelium versus time in high KCl (G) or *kcnh2a*$^{lof/lof}$ (I). Insets: Condition-specific depiction of K^+ flux across epithelia. (**H** and **J**) Position of apical epithelial cells relative to wound versus time of Ca^{2+} wavefront (triangle) or flashes (cross) activation in high KCl (H) or *kcnh2a*$^{lof/lof}$ finfolds (J). Shades: 25 to 75% percentile. Cyan lines: diffusive fit in linear scale; linear fit in log-to-log scale (0.1 to 5 s). Cyan dash: diffusive fit at 0.1 to 20 s. Error: 95% CI of parameter fits. R^2: goodness of fit. *N*: number of larvae [(F), (G), (I), and (K)]; *n*: number of cells [(C), (F), (H), (I), (J), and (K)]. Scale bars, 50 μm.

Membrane potential regulates proliferation associated with tissue growth

Our results show that electrical signals in the form of fast tissue-wide V_{mem} depolarization arise upon organ injury. However, successful organ repair often relies on cell proliferation to recover functionality, which occurs over hours or even days postdamage (*72*, *73*). While electrical cues have been shown to trigger diverse cell behaviors in injured tissues (*2*–*6*, *22*–*24*, *28*–*30*,*74*), it remains unclear how cells can use fast changes of electrical signals to control slower organ growth. To fill this gap, we extended our experimental assay to explore how spatial V_{mem} changes triggered by injury could be linked to proliferation and organ growth (Fig. 3A).

After injury at 2 days postfertilization, the zebrafish finfold regrows within 3 days, not only recovering the lost part of the tissue but also compensating for developmental time by adjusting its growth rates (*45*, *72*, *75*). In effect, upon amputation, this organ "catches up" with its developmental age (5 days postfertilization), reacquiring functional size, architecture, and patterning, without defects or tumor formation (Fig. 3B and fig. S8, A to D) (*45*).

Damage-induced proliferation in the 2-days postfertilization larval fin is reported to occur mostly within the first day postinjury (*72*). By revisiting such data and labeling proliferative cells [5-ethynyl-2′-deoxyuridine (EdU^+)] in 2-hour intervals after injury, we found two proliferation peaks occurring within 13 hours across all finfold layers (Fig. 3, C to E): the first at 1 to 3 hours postamputation, spanning ~200 μm from the wound into the tissue (fig. S8, E and F), and the second at 7 to 9 hours postamputation, occurring only at distant positions from the wound (fig. S8, E and F). Spatial analysis further showed that between 1 and 3 hours postamputation, proliferation is higher within ~100 μm from the wound when compared to 7 to 9 hours postamputation (Fig. 3, E and F, and fig. S8, E and F).

The similar length scales between cell proliferation and V_{mem} depolarization in injured finfolds at 1 hour postamputation (100 μm, considering the larger changes in membrane depolarization; Fig. 1K) made us ask whether the electrical signals arising upon tissue injury could trigger proliferation. To test this, we measured proliferation and finfold size (Fig. 3A) under the ion flux perturbations tested previously. In $kcnh2a^{lof/lof}$ and FK506-treated larvae, both V_{mem}-hyperpolarizing conditions (*47*, *54*, *68*–*71*), the first proliferative peak occurring after injury (1 hour postamputation) was impaired without affecting proliferation at 7 hours postamputation (Fig. 3G and figs. S9F and S10, F and G). This impairment is also evident spatially, as no increase in proliferation is observed within 100 μm from the wound (Fig. 3H) when compared to WT. The lack of cell proliferation at 1 hour postamputation resulted in finfold length defects observable in the first day postamputation (figs. S9, A to C′, and S10, A to C′), ultimately leading to smaller larval fin sizes at 3 days postamputation (Fig. 3, I and J, and figs. S9, B, D, and E, and S10, B, D, and E). These phenotypes appear specific to damaged finfolds because the perturbations applied did not influence developmental proliferation or length of uninjured larval fins (figs. S9, A, B, and G, and S10, A, B, and H).

In contrast, to understand whether tissue-wide V_{mem} depolarization (fig. S6E) can trigger proliferation and organ growth independently of wounding, we exposed 2-days postfertilization zebrafish to high KCl for 1 hour (Materials and Methods). Unexpectedly, in the absence of injury, this treatment led to larval fin overgrowth (Fig. 3, K and L, and fig. S11B; 10% length increase) by amplifying finwide proliferation (Fig. 3, M and N, and fig. S11E). Longer KCl treatment (Materials and Methods) also led to longer finfolds (fig. S11F). In addition, upon injury at 2 days postfertilization, 1 hour of high KCl exposure still resulted in recovery of larval fin size at 5 days postfertilization (fig. S11, A to D). Inducing V_{mem} depolarization by KCl treatment was able to rescue the $kcnh2a^{lof/lof}$ finfold regrowth phenotype (Fig. 3, I and J, and fig. S9H), suggesting that $kcnh2a^{lof/lof}$ mutants are unable to trigger cell proliferation at 1 hour postamputation due to the hyperpolarized V_{mem} state, potentially caused by increased cellular K^+ efflux (*70*, *71*).

Overall, our results indicate that electric signals resulting from wounding trigger the initial proliferative cellular responses necessary for complete larval fin repair, and tissue-wide V_{mem} depolarization is sufficient to induce cell proliferation independently of wounds within 1 hour.

VSP relays V_{mem} depolarization into cell proliferation

Next, we set out to investigate the molecular effector that could sense V_{mem} depolarization, transmitting such signals intracellularly to initiate proliferation. Therefore, we probed the literature for candidate membrane proteins with voltage sensing domains, coming across the conserved protein Voltage Sensing Phosphatase, VSP (*76*), encoded in zebrafish by *tpte* (*77*, *78*). This integral membrane protein becomes active when its N-terminal voltage sensor domain detects large V_{mem} depolarization. Its C terminus encodes a phosphatase, having as substrates the lipids phosphatidylinositol (3, 4, 5)-trisphosphate (PIP3) and phosphatidylinositol 4,5-bisphosphate (PIP2). VSP changes conformation upon membrane depolarization above ~+40 mV, activating its cytosolic phosphatase and dephosphorylating PIP3 and PIP2 (*76*, *79*–*81*). In vitro studies have suggested that changes in V_{mem} can trigger proliferation through remodeling of membrane phospholipids (*82*), but the molecular sensor and effector of V_{mem} changes remain unknown. Consequently, we hypothesized that VSP senses and transduces the injury-driven V_{mem} depolarization signals (Fig. 1H), leading to the observed cell proliferation at 1 hour postamputation (Fig. 3C).

We found that VSP is expressed in the 2-days postfertilization larval caudal finfold, being localized at the membranes of the apical epithelial cells (Fig. 4A). This prompted us to further investigate whether proliferation is spatially biased across the two epithelial finfold layers. While during finfold development, proliferation occurs mostly in the basal epithelium (*83*), upon injury, the number of apical epithelial cells undergoing division unexpectedly increases, both at 1 and 7 hours postamputation (Fig. 4B, cut). In contrast, the number of proliferating basal cells remains unchanged or even decreases upon injury (Fig. 4B).

To test whether VSP is responsible for the proliferative response occurring in the apical epithelial layer upon injury, we generated a *tpte* CRISPR mutant that carries a stop codon in the 5′ region of its coding sequence ($tpte^{cbg22}$; Fig. 4C). While homozygous *tpte* mutants (i.e., $tpte^{-/-}$) lack VSP expression (Fig. 4D, fig. S12A), they do not show evident developmental defects (fig. S12, B to E). In contrast, injured $tpte^{-/-}$ mutants are unable to successfully regrow their larval fins by 3 days postamputation (Fig. 4, I and J, and fig. S12, E to G), similar to the observed $kcnh2a^{lof/lof}$ phenotypes (Fig. 3, I and J).

Notably, within the first 11 hours postamputation in injured $tpte^{-/-}$ finfolds, we find only the first proliferative peak to be absent (1 to 3 hours postamputation; Fig. 4, E to H, and fig. S12, I and J), while the Ca^{2+} wavefront remains unaffected (fig. S12H), indicating that early injury responses still occur. We confirmed the specificity

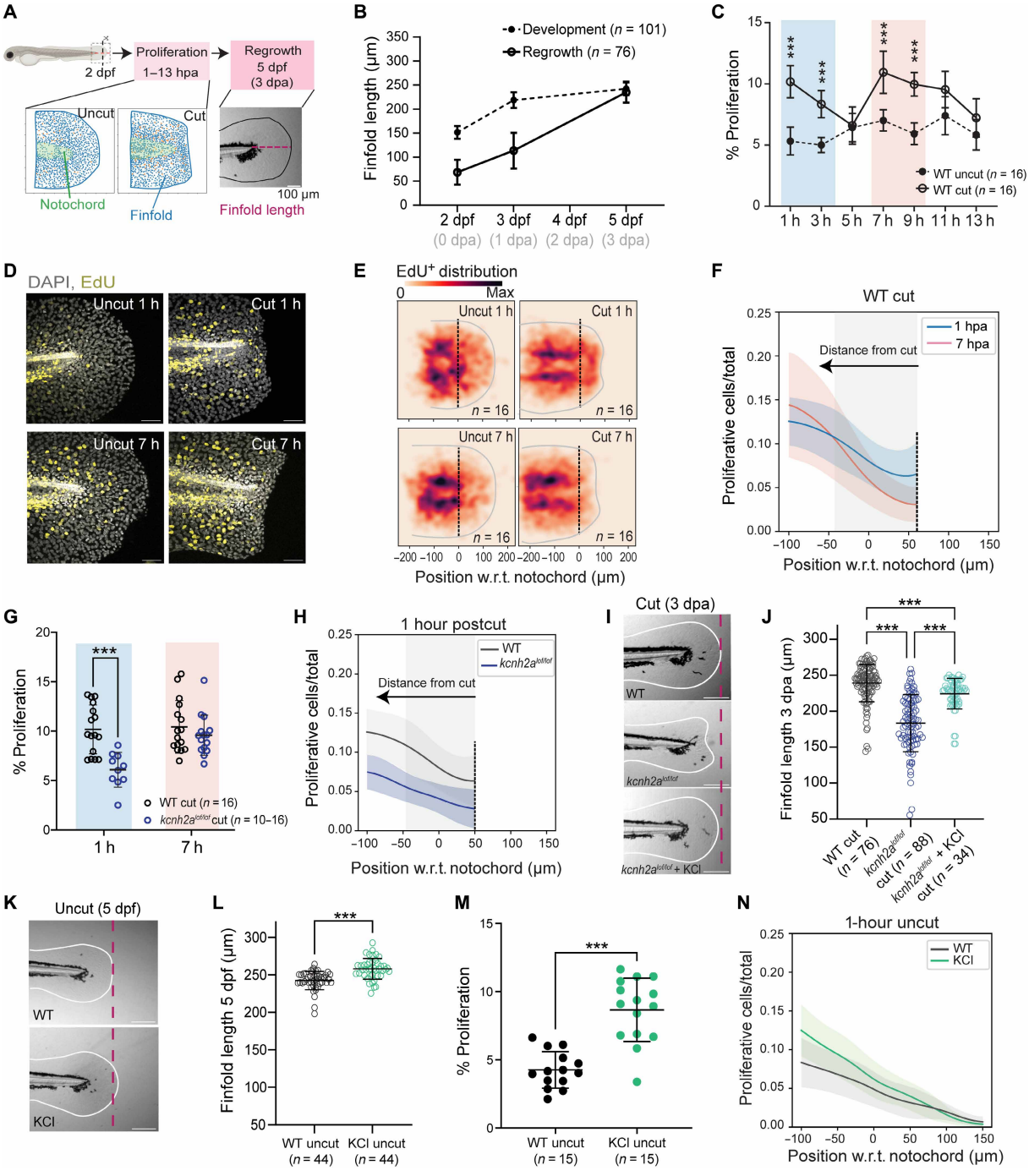

Fig. 3. V_{mem} changes regulate cell proliferation at 1-hour postinjury. (**A**) Finfold proliferation and regrowth assays. (**B**) Finfold lengths in development versus injury, 2 to 5 days postfertilization. (**C**) Percentage of proliferative (EdU^+) per total cells [labeled with 4′,6-diamidino-2-phenylindole ($DAPI^+$)] in uncut versus cut finfolds from (D). Shades: proliferation peaks. Mean ± 95% CI. (**D**) Immunostainings labeling proliferative cells (yellow; EdU^+) and nuclei (gray; DAPI). (**E**) Heatmaps of finfold proliferation distribution under cut and uncut conditions. Outline: average finfold boundary. Dash: notochord tip. (**F**) Fraction of proliferative cells versus finfold position in cut finfolds, at 1 and 7 hours postamputation (hpa). Note increase within 100 µm from cut (gray; rectangle) in 1 versus 7 hours postamputation. (**G**) Percentage of proliferative cells per total in *kcnh2a*$^{lof/lof}$ versus WT, at 1 and 7 hours postamputation. Mean ± 95% CI. (**H**) Fraction of proliferative cells versus position in WT versus *kcnh2a*$^{lof/lof}$, at 1 hour postamputation. (**I**) WT, *kcnh2a*$^{lof/lof}$, and *kcnh2a*$^{lof/lof}$ treated with KCl, at 3 days postamputation (dpa). (**J**) Finfold lengths of WT versus *kcnh2a*$^{lof/lof}$ versus *kcnh2a*$^{lof/lof}$ treated with KCl, at 3 days postamputation. (**K**) Uncut finfolds in WT and KCl-treated larvae. (**L**) Finfold lengths in uncut WT versus KCl-treated larvae. (**M**) Percentage of proliferative cells in uncut WT versus KCl-treated larvae. (**N**) Fraction of proliferative cells versus position in uncut WT and KCl-treated larvae. Scale bars, 50 µm [(D), (G), and (M)] and 200 µm [(I) and (K)]. [(I) and (K)] pink dash: 5 days postfertilization uncut WT finfold length. [(F), (H), and (N)] line and shade: mean ± SD. Zero: notochord tip. [(B), (J), (L), and (M)] mean ± SD. All statistics: ***$P \leq 0.001$; [(C), (G), and (J)] two-tailed, unpaired, nonparametric Mann-Whitney tests; (L) two-tailed, unpaired, parametric *t* test. *n*: number of embryos. [(F) and (H)] Dash line indicates cut position. w.r.t., with relation to; h, hours.

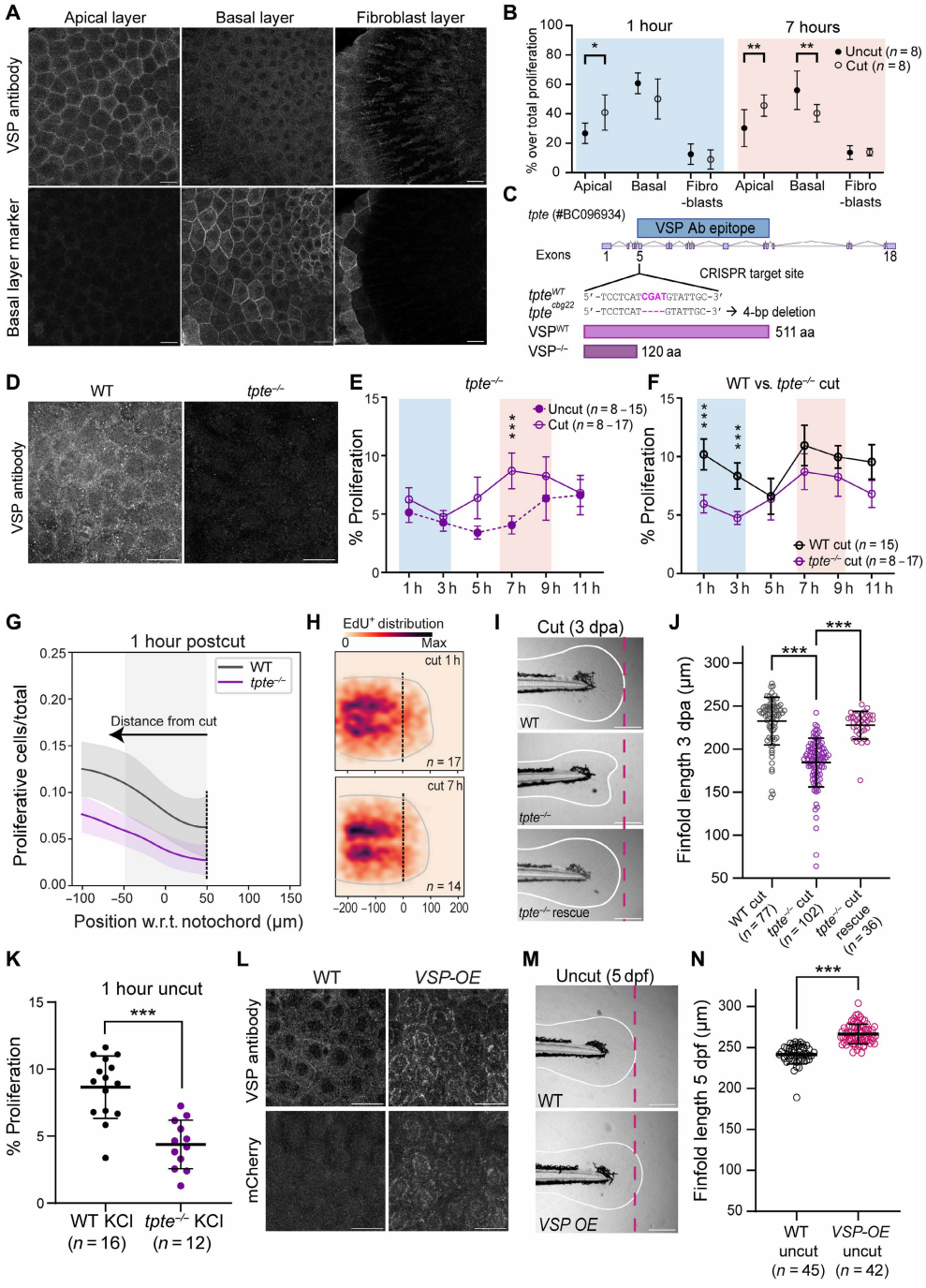

Fig. 4. VSP translates changes in V_{mem} into proliferation. (**A**) VSP immunostainings in 2-days postfertilization (dpf) apical and basal finfold epithelial layers (single frames). Basal layer marker: tp63:CAAX-GFP. (**B**) Percentage of proliferating cells in each finfold layer per total proliferation under uncut and cut conditions, at 1 and 7 hours. Mean ± 95% CI. (**C**) *tpte* genomic structure. Target sequence of *tpte*^{cbg22} in exon 5 with truncated VSP protein. Anti-VSP epitope is indicated. Ab, antibody; aa, amino acids. (**D**) VSP immunostainings in 2-days postfertilization WT and *tpte*$^{-/-}$ finfolds (max intensity projections). (**E** and **F**) Proliferation percentage in *tpte*$^{-/-}$ uncut versus cut (E) or WT versus *tpte*$^{-/-}$ (F) finfolds, 1 to 11 hour postamputation. Mean ± 95% CI. Shades: WT proliferation peaks from Fig. 3C. (**G**) Fraction of proliferative cells versus position in WT versus *tpte*$^{-/-}$ finfolds, at 1 hour postamputation. Zero: notochord tip. Gray area: 100 µm from cut. Line and shade: mean ± SD. Dash: cut position. (**H**) Heatmaps of finfold proliferation distribution in *tpte*$^{-/-}$, 1 and 7 hours postamputation. Outline: average finfold boundary. Dash: notochord tip. (**I**) WT, *tpte*$^{-/-}$, and *tpte*$^{-/-}$ rescue finfolds, 3 days postamputation. Outlines: finfold boundary. Pink dash: 5-days postfertilization uncut WT finfold length. (**J**) Finfold lengths' comparison between WT, *tpte*$^{-/-}$, and *tpte*$^{-/-}$ rescue, at 3 days postamputation. (**K**) Percentage of proliferative cells in *tpte*$^{-/-}$ versus WT, KCl-treated larvae. Mean ± 95% CI. (**L**) VSP immunostaining in VSP overexpression transgenics (VSP-OE and mCherry) and WT, 2-days postfertilization apical epithelium. Maximum intensity projection of two planes. (**M**) Uncut finfolds in WT and VSP-OE larvae. (**N**) Finfold lengths from WT versus VSP-OE. Scale bars, 20 µm [(A), (D), and (L)] and 200 µm [(I) and (M)]. *n*: number of embryos. [(J), (K), and (N)] mean ± SD. All statistics: **P* ≤ 0.05, ***P* ≤ 0.01, and ****P* ≤ 0.001; [(B), (E), (F), and (K)] two-tailed, unpaired, nonparametric Mann-Whitney tests; [(J) and (N)] two-tailed, unpaired, parametric *t* tests.

of the *tpte*$^{-/-}$ phenotypes by combining transgenics that conditionally overexpress WT VSP with *tpte*$^{-/-}$ (Materials and Methods), observing a rescue of the injury-triggered finfold size defects at 3 days postamputation and excluding potential off-target effects (Fig. 4, I and J, and fig. S13, A to C, *rescue*).

The above observations suggest that loss of VSP in *tpte*$^{-/-}$ impairs intracellular transduction of V_{mem} depolarization triggered by finfold injury, decreasing cell proliferation at 1 hour postamputation and causing larval fin size defects by 3 days postamputation (fig. S12, L to O). To confirm that VSP is the molecular effector that relays V_{mem} depolarization into cell proliferation independently of injury, we triggered tissue-wide V_{mem} depolarization by high KCl exposure in *tpte*$^{-/-}$ uncut larval fins. Here, mutant finfolds do not display increased proliferation in contrast to WT (Fig. 4K and fig. S12K). We conclude that VSP specifically senses and converts V_{mem} depolarization signals into cell proliferation.

Last, to test whether modulating VSP activity can trigger organ growth independently of injury, we generated conditional transgenics that overexpress a modified version of VSP upon heat shock (VSP-OE; Materials and Methods). This enhanced VSP version has increased membrane recruitment and phosphatase activity, being more efficient in depleting PIP2 from the plasma membrane (*81*). Overexpressing this form of VSP in uncut 2-days postfertilization larval fins (Fig. 4L, fig. S13, H to J, and Materials and Methods) results in longer finfolds at 5 days postfertilization (Fig. 4, M and N, and fig. S13D), presenting a similar 10% finfold length increase such as in KCl-treated larvae (Fig. 3L). Analogously, activating VSP-OE in injured fins also leads to finfold size recovery at 3 days postamputation (fig. S13, D to G). Together, our experiments show that VSP is the molecular effector that couples membrane potential depolarization signals into cell proliferation, being both necessary and sufficient to achieve complete larval fin repair.

DISCUSSION

Our work reveals that the earliest organ-scale wound responses are closely instructed by the intrinsic bioelectrical state of tissues, conferred by dynamic regulation of the cellular membrane potential. Tissue-scale V_{mem} depolarization occurs immediately upon organ injury, initiates proliferation, and, consequently, fast-tracks organ repair. These V_{mem} changes are sensed by a voltage-sensing protein, VSP, which converts V_{mem} depolarization into intracellular chemical responses, resulting in controlled proliferation. This coupling primes the injured organ for functional size recovery.

Using subsecond-resolved live imaging while precisely injuring zebrafish larval fins, we measured unprecedented tissue-scale V_{mem} and Ca^{2+} dynamics that constitute the fastest detected organ injury signals yet (100 ms) (Fig. 1, C to F and H and I). When combining these measurements with a developed electrodiffusive model (Fig. 2, A to D), we captured multitimescale dynamics of the early injury signals in tissues, inaccessible in previous frameworks—often these are modeled using equations borrowed from single neuron dynamics (*10*, *84*, *85*). Our approach uncovered two timescales occurring after tissue damage: a millisecond response under quasistatic ionic concentration profiles, due to V_{mem} short circuiting caused by injury, and a second response occurring in the seconds after, resulting from the electrochemical interplay of ion diffusion and transport across the larval fin's epithelium. Together, these two timescales provide the physical basis for the initiation and propagation of wound currents and postinjury intracellular Ca^{2+} signaling in tissues, two damage responses highly conserved across eukaryotes (*21*, *23*–*25*, *30*, *33*–*38*, *43*). Our theoretical framework also clarified that for these general injury-driven tissue responses to occur, the key parameters driving the observed spatiotemporal dynamics are the tissue's permeability to ions, regulated usually through tight junctions (*17*) and the organ's IF ionic concentration.

Despite the V_{mem} of both larval fin epithelial layers becoming depolarized upon injury, we found that depolarization-induced cell proliferation occurs solely in the apical epithelial layer, due to VSP expression (Fig. 4A). While the layer-specific expression of VSP remains enigmatic, understanding whether its location is restricted to tissues that are injury prone will likely be relevant to enhance the proliferative capability of tissues with low regenerative potential. Furthermore, as VSP expression is conserved across tissues and species, including humans (*76*, *86*), its functional role is likely to be broad and not confined to epithelia or zebrafish larvae.

Our data further show that VSP acts within 1 hour postinjury to transduce electrical signals into cell proliferation (Fig. 4, E to G), suggesting a transcription-independent downstream cascade. Previous in vitro studies have connected membrane depolarization to proliferation through lipid remodeling and K-ras signaling (*82*). Future work addressing the possible link between VSP activation, PIP membrane levels, and mitogen-activated protein kinase spatiotemporal dynamics will enable a closer investigation of the dynamics of cell proliferation activation in injured fins. While here we uncovered that early organ-wide proliferation dynamics are controlled by electrical signals at 1 hour postinjury, we also observed that at 7 hours postinjury, cells proliferate independently of the described voltage-sensing mechanism (Fig. 4F). Given the timescale, this second proliferative peak is consistent with transcriptional activation of proregenerative signaling (*45*, *75*, *87*). The rapid onset of proliferation at 1 hour postdamage proved essential for the organ to recover its complete morphology 3 days later, suggesting that such early injury signals may be important for further downstream processes.

We observed similar phenotypes in *tpte*$^{-/-}$ and *kcnh2a*$^{lof/lof}$ mutants: In both genetic backgrounds, cell proliferation is impaired at 1 hour postinjury, resulting in incomplete organ growth (Figs. 3G and 4F). A working hypothesis is that in both cases, VSP cannot relay the membrane depolarization signal intracellularly into cell proliferation. While in *tpte*$^{-/-}$, this is due to lack of VSP expression, and in *kcnh2a*$^{lof/lof}$, due to the nature of this gain-of-function mutation, cellular K^+ efflux should be generally increased, hyperpolarizing the resting membrane potential of the tissue (*47*, *54*, *68*–*71*). Given this hyperpolarized V_{mem} baseline, upon wounding, the induced V_{mem} depolarization may not be sufficient to trigger VSP activation, known to occur at a V_{mem} threshold of ~+40 mV in zebrafish (*76*, *79*, *81*). Furthermore, our current interpretations of the *tpte*$^{-/-}$ and *kcnh2a*$^{lof/lof}$ proliferation phenotypes are based on the level of V_{mem} depolarization that the injury triggers. In WT, this depolarization seems to be large enough to trigger VSP at least in the first 100 μm from the wound and at least for 5 s, as highlighted by our Voltron2 experiments (Fig. 1, K and J). We cannot, however, exclude that lower-than-detected V_{mem} depolarization can trigger VSP activity, resulting in apical cell proliferation further away from the wound and justifying the *tpte*$^{-/-}$ spatial distribution proliferation phenotypes at 1 hour postamputation.

Both *kcnh2a*$^{lof/lof}$ and FK506 treatments have been found to promote fin outgrowth in adult zebrafish and other fishes (*47*–*49*, *51*, *52*, *54*). This apparent discrepancy with our larval fin findings (Fig. 3J) could be due to differences in the cell types that respond to injury: Our larval system regrows by essentially promoting epithelial proliferation (Fig. 4B), instead of a classic dedifferentiated, proliferative mesenchymal blastema structure (*73*, *88*). Deciphering the electrochemical dynamics of V_{mem} and ion fluxes in the adult mesenchymal blastema, especially considering the timescale of that regenerative process (2 weeks), is an exciting frontier to be explored.

Last, inducing tissue-wide membrane depolarization by KCl treatment or mimicking such an effect by overexpressing VSP with enhanced activity led to longer finfolds (Fig. 3L and 4N). We deem that controlled cell proliferation upon V_{mem} depolarization could indeed act as a general mechanism affecting organ size beyond contexts involving injury and repair.

Building on recent discoveries of bioelectrical processes at the heart of critical cellular and organismal functions (*8*, *9*, *11*, *30*, *52*, *53*, *84*, *89*, *90*), our work suggests that electrical regulation at the collective is a prevalent physically driven mechanism for organs in the need of rapid cell-cell communication and signal transduction. Our study opens an avenue for resolving the spatiotemporal interplay between fast electrical signals and slower biochemical signaling underlying organ repair mechanisms.

MATERIALS AND METHODS

Ethics statement

This study followed European Union directives (2010/63/EU) and German law, with license no. TVV52/2021—"Generierung von Zebrafischlinien zur Untersuchung der Größe und Form von Organen und Organellen." Genetic engineering work was carried out in an S1 area [Max Planck Institute of Molecular Cell Biology and Genetics (MPI-CBG), S1-Labore 4., Az.: 54-8451/103, project leader R. Mateus], following guidelines according to section 21, paragraph 1 of the German Genetic Engineering Act, and within projects 01-03 from the Mateus laboratory, according to section 28 of the German Genetic Engineering Safety Ordinance.

Zebrafish lines and maintenance

All zebrafish (*Danio rerio*) lines were maintained in a recirculating system with a 14 hours/day, 10 hours/night cycle at 28°C. Crosses were performed with 3- to 12-month-old adults. Embryos were kept in E3 zebrafish embryo medium (*91*) at 28.5°C until the desired developmental stage was reached. We used the following transgenics either in WT AB or *longfin*$^{t2/t2}$ (i.e., *kcnh2a*$^{lof/lof}$) (*92*) backgrounds: *Tg(−8.0cldnb:lynGFP)*^{zf106} (*93*) (i.e., claudinb:Lyn-GFP) for labeling the finfold's apical epithelial cell layer (periderm); *Tg(tp63:CAAX-GFP)*^{mdi2013Tg} (*94*) for labeling the finfold's basal epithelial cell layer; and *Tg(actb2:LY-tdTomato)*^{zf2254Tg} (i.e., b-act:lyn-tdTomato) to label all membranes (*95*).

tpte^{cbg22} mutant

tpte^{cbg22} CRISPR mutants were generated as described previously (*96*). Briefly, trans-activating CRISPR RNAs (tracrRNAs) were designed for specific loci of the *tpte* gene (Ensembl ID: ENSDARG00000056985) using predesigned crRNAs (Integrated DNA Technologies). Several crRNAs were tested for ribonucleoprotein (RNP) mutagenesis and were chosen considering where the start codon is located, as well as high on-target and low off-target scores. The most efficient crRNA tested was located on exon 5 of the zebrafish *tpte* canonical transcript, with target sequence 5′-CACGGAGCAATACATCGATG-3′ (IDT, Dr.Cas9.TPTE.1.AC). The crRNA was annealed with an equal molar amount of tracrRNA (IDT, #1072533) and diluted to 57 μM Duplex buffer (IDT, #11-01-03-01), generating the single guide RNA (sgRNA). The sgRNA was mixed with the Cas9 protein (Alt-R S.p. Cas9 Nuclease V3, 1081058, IDT; 61 μM stock) in equimolar amounts, generating a 28.5 μM RNP solution. To improve mutagenesis efficiency, the mix was kept overnight at −20°C before injections the following day. One-cell stage *Tg(ubb:GCaMP6f)*^{m1299} embryos were injected with 1 nl of the RNP mix and grown to adulthood. Founder fish containing frameshift mutations were identified by genotyping the resulting F1 progeny, resulting from outcrosses with WT AB fish. The mutant fish show a 4–base pair (bp) deletion in exon 5 (Fig. 4C).

Transgenic line generation

All transgenesis was performed using the Tol2 transposon system and Gateway cloning (*97*, *98*) technology. For *Tg(Hsp70:CiDr-VSP-wt-mCherry)*^{cbg24Tg}, we used the CiDr-VSP-wt-mCherry pcDNA3.1 plasmid81 as a template for subcloning. For *Tg(Hsp70:CiDr-VSP-L223f-mCherry)*^{cbg23Tg} generation, we used the CiDr-VSP-L223F-mCherry pcDNA3.1 plasmid (Addgene, #140892) (*81*) as a template for subcloning. The CiDr-VSP-WT-mCherry and the CiDr-VSP-L223F-mCherry fragments were amplified using primers containing attB1 and attB2 sites: 5′-GGGGACAAGTTTGTACAAAAAAGCAGGCTTA-atggagggattcgacggttca-3′ (forward) and 5′-GGGGACCACTTTGTACAAGAAAGCTGGGTTttactt-gtacagctcgtccatgcc-3′ (reverse). The 2494-bp amplified products were purified using a polymerase chain reaction (PCR) cleanup kit (Promega, #A9281) and recombined with pDONOR221 [Tol2kit, #208 (*98*)] in a BP reaction (BP Clonase II enzyme mix, Invitrogen, #11789020). The resulting middle entry clones, pME_CiDr-VSP wt-mCherry and pME_CiDr-VSP L223F-mCherry, were then recombined in independent LR reactions (LR Clonase II Plus enzyme, Invitrogen, #12538120) using p5E-hsp70 (Tol2kit, #222), pDEST-Tol2pA_myl7:EGFP (R4-R3) (Tol2kit, #395), and p3E-polyA (Tol2kit, #302), to generate the final constructs, T2_Hsp70:CiDr-VSP-wt-mCherry_pA_myl7:GFP and T2_Hsp70:CiDr-VSP-L223F-mCherry_pA_myl7:GFP. One-cell stage WT AB embryos were injected with 25 pg of the final construct, 25 pg of Tol2 transposase mRNA, and 10% phenol red. At 2 days post-fertilization, injected embryos were screened for GFP expression in the heart (driven by the *myl7* selection marker) using an Olympus SZX16 fluorescence microscope and subsequently grown to adulthood. Founder fish were identified by screening F1 progeny for selection marker fluorescence, resulting from outcrosses with WT AB fish.

For the *Tg(ubb:GCaMP6f)*^{m1299} line, an attB1 primer (5′-GGGGACAAGTTTGTACAAAAAAGCAGGCTGAACCGTCAGATCC-GCTAG-3′) including Kozak sequence was used to amplify GCaMP6f (Addgene, #40755 pGP-CMV-GCaMP6f) (*99*). The *ubb* promoter [3.5 kb (*100*); Addgene, #27320] was inserted into the pENTR5' plasmid. pENTR5' (*ubb*), pME (GCaMP6f), and pENTR3' [polyadenylate (polyA)] sequences were then cloned into the pDestTol2pA2 plasmid via an LR clonase reaction (Gateway LR Clonase Plus enzyme, Thermo Fisher Scientific, #12538120). Plasmid DNA (25 ng/μl) and Tol2 transposase mRNA (50 ng/μl) were coinjected into single-cell stage embryos (nacre$^{+/-}$ background). F2 or later generations in WT AB background were used for this study's data acquisition.

Genotyping

Genomic DNA from clipped tail fins from adult zebrafish was extracted using the Kapa Express Extract kit (Kapa Biosystems) according to the manufacturer's protocol. This was followed by performing PCR with KAPA2G Robust HotStart ReadyMix (Kapa Biosystems). For *tpte*^{cbg22} genotyping, the following primers were used: 5′-GTTTTCGGTGAGTGGCATAC-3′ (forward) and 5′-GTTACTGTTAGTCTTACGAGC-3′ (reverse). Resulting PCR products from either mutant were sent for sequencing and sequences analyzed using SnapGene (v7.1).

For *longfin*^{t2} genotyping, the following primers were used on the basis of (*52*): *wt_breakp_fwd*, 5′-cgttgaatcaccgttgaaatgcc-3′; *lof_breakp_fwd*, 5′-ggccttgttaagctcaagtg-3′; and *breakp_rev*, 5′-ggtttcgatatgtggcagatttaagg-3′. Primer pairs were used in combination in two concomitant PCRs (alternating only the forward primer), resulting in PCR products of 522 bp (*wt_breakp_fwd* and *breakp_rev*, amplifying a WT sequence) and 526 bp (*lof_breakp_fwd* and *breakp_rev*, amplifying the *lof* sequence) for heterozygous fish, and only the 526-bp product for homozygous fish. Given that *lof* is a dominant mutation (*92*), adult fish with fins that displayed WT dimensions were phenotyped and not genotyped. Genotyping was performed to identify heterozygous and homozygous fish despite phenotypic differences in fin lobe size.

Voltron2 cloning, mRNA synthesis ,and embryo microinjection

The construct pCS2 + _Voltron2 was generated by subcloning from pGP-pcDNA3.1 Puro-CAG-Voltron2 (Addgene, #172909) (*61*) with Gateway technology (*97*, *98*). Briefly, the Voltron2 fragment was amplified using primers containing attB1 and attB2 sites: 5′-GGGGACAAGTTTGTACAAAAAAGCAGGCTTAatggctgacgtggaaaccg-3′ (forward) and 5′-GGGACCACTTTGTACAAGAAAGCTGGGTTttacacctcgttctcgtagcagaac-3′ (reverse). The 1720-bp amplified product was purified using a PCR cleanup kit (Promega, #A9281) and recombined with pDONOR221 [Tol2kit, #208 (*98*)] in a BP reaction (BP Clonase II enzyme mix, Invitrogen, 11789020). The generated middle entry clone, pME_Voltron2, was then recombined in a LR reaction using pCSDEST (Tol2kit, #201) (LR Clonase II Plus enzyme, Invitrogen, 12538120) to generate pCS2 + _Voltron2. To make Voltron2 mRNA, the pCS2 + _Voltron2 vector was linearized with NotI (New England Biolabs) and transcribed using the SP6 mMessage Machine Kit (Invitrogen, #AM1340) according to the manufacturer's instructions. The same procedure was applied for Tol2 transposase mRNA synthesis, generated from a pCS2FA-transposase plasmid (*98*). mRNAs were aliquoted and stored at −70°C until use. One-cell stage WT AB or claudinb:lyn-GFP transgenic embryos were injected using standard procedures with 150 to 200 pg of Voltron2 mRNA. Embryos were left to develop at 28.5°C until the desired stage. A PV-820 Pico-injector (World Precision Instruments) and a Narashige micromanipulator were used for microinjection.

GAP27 peptide heart injections

To inhibit pore formation of gap junctions, 0.5 mM Gap27 peptide (700 pg per embryo) (Tocris, #1476) was injected in the heart of 2-days postfertilization larvae as previously described (*101*). Control embryos were injected with a mix of water and phenol red without GAP27 peptide. Briefly, 1-mm borosilicate glass needles (Premium thin Wall Borosilicate Capillary Glass, OD 1.0 mm, ID 0.78 mm, Harvard Apparatus, #640778) were pulled with a TCF Sutter "9" to the inner diameter of 15 µm, with a bevel at 30°C and a spike, to facilitate piercing into the zebrafish skin. Embryos were anaesthetized with 20 mg/ml of tricaine (*102*) and were placed against a glass slide in a plastic petri dish with the head facing the slide, the needle was positioned at a 30° to 45°C angle with respect to the heart, and it was introduced in the atrium without piercing the yolk. Embryos were imaged 5 hours after injection due to known connexin turnover (*103*, *104*). A PV-820 Pico-injector (World Precision Instruments) and a Narashige micromanipulator were used for microinjection. Two independent experiments were performed, with different biological replicates per condition.

Chemical treatments

Before all chemical treatments, embryos were manually dechorionated.

Voltron2 labeling with Janelia Fluor 552

Embryos injected with Voltron2 mRNA were incubated with 500 nM Janelia Fluor Dye 552 (JF552)–HaloTag ligands in E3 with 0.5% dimethyl sulfoxide (DMSO) at 36 hours postfertilization for 12 hours. The dye was then washed twice for 10 min with 4 ml of E3 with 0.5% DMSO. Embryos were screened for fluorescence (Olympus SZX2 with a X-Cite Series 120PC QLED lamp, ET 630/75 bandpass) before mounted for live imaging in 0.5% low-melt agarose (E3).

Ca^{2+}-free E3 medium

Ca^{2+}-free 1× E3 medium (dissolved from 60× solution: 34.8 g of NaCl +1.6 g of KCl + 9.78 g of $MgCl_2{\cdot}6H_2O$ in 2 liters of H_2O) was prepared and used to incubate embryos for 5 hours before imaging. Up to 40 embryos were incubated per 15 ml of medium. Embryos were mounted for live imaging in 0.5% low-melt agarose (Ca^{2+}-free E3).

High KCl supplement

KCl-supplemented medium consists of highly concentrated KCl in E3 medium [135 mM, ~282 mosmol/liter, and considered isotonic to the finfold's IF (*30*)] (5.032 g of KCl dissolved in 500 ml of E3, Supelco, CAS #7447-40-7). For Ca^{2+} wave imaging, two treatment conditions were used, where no harmful side effects were noted in embryos: i) overnight incubation and ii) 1-hour incubation. For the overnight treatment, embryos were incubated in KCl-supplemented medium at 36 hours postfertilization for 12 to 18 hours until imaging of Ca^{2+} wave (Fig. 2, G and H). Up to 40 embryos were incubated per 15 ml of KCl-supplemented medium. After the incubation, embryos were mounted for live imaging in 0.5% low-melt agarose (made with KCl-supplemented E3 medium). Under this overnight KCl treatment condition (without cutting), we also observed longer caudal finfolds at 5 days postfertilization (fig. S11F) that suggests that an increase in cell proliferation took place.

To capture proliferation events in response to depolarization, we treated uncut embryos with 135 mM KCl for 1 hour and cut embryos for 1 hour before amputation and 1 hour after amputation. Both treatments were followed by EdU (see below). We also examined the injury-induced Ca^{2+} wave response under this 1 hour KCl treatment condition. To do this, we mounted 48-hours postfertilization embryos in 0.5% low-melting agarose (E3 medium) and then perfused in the dish KCl-supplemented medium at 1 hour before UV-laser microdissection and live imaging. Under control conditions, only E3 medium was perfused. Under this condition, we found that Ca^{2+} wave still stops at >300 µm away from the cut (fig. S11, G and H), agreeing with the threefold increase displayed under the overnight

KCl treatment condition. While osmotic effects may occur after the injury electric responses [90 s to minute timescale (*30*)], the KCl treatment(s) applied here did not disrupt regeneration and promoted finfold growth (Fig. 3, K to N, and fig. S11).

For finfold regrowth assays, uncut embryos were incubated with KCl for 1 or 12 hours, and cut embryos were further incubated for 1 hour following amputation. Embryos were then returned to E3 medium.

For Voltron2 imaging, KCl was supplemented during spinning disk live imaging by pipetting a small volume (50 µl) of 2700 mM KCl in E3 medium to a large volume (950 µl) of E3 medium, with the fish mounted in 0.5% low-melting agarose (in E3 medium), leading to a final concentration of 135 mM KCl. For this condition, a fraction of embryos does not survive the high KCl shock, when pipetting was too fast or applied too close to the mounted fish. Only embryos that do not show an adverse effect 1 hour after KCl application were included in data analysis (fig. S6E and S15).

FK506

Embryos were incubated with 10 µM FK506 (Sigma-Aldrich, #F4679) (*105*) at 36 hours postfertilization for 12 to 18 hours before live imaging. Up to 40 embryos were incubated per 15 ml of FK506-supplemented medium. After the overnight incubation, embryos were mounted for live imaging in 0.5% low-melting agarose (FK506-supplemented E3 medium). For regeneration and proliferation assays, FK506 was washed at 1 hour postamputation.

Spinning disk live imaging and UV-laser microdissection

Before imaging, embryos were anesthetized with 0.1% Tricaine (MS-222, Sigma-Aldrich) dissolved in E3 medium. Anesthetized embryos were mounted in 0.5% low-melt agarose (Sigma-Aldrich) containing 0.1% Tricaine in glass bottom dishes (CellView). Live imaging was performed at 28.5°C (stage-top incubator) using a spinning disk confocal microscope equipped with a Yokogawa CSU-X1 scan head (25× water immersion objective and 0.8 numerical aperture, paired with an objective heater also at 28.5°C) connected to a Zeiss camera (Axiocam 705 mono). Images were acquired using the Zeiss ZEN (3.2 Blue) software.

Caudal finfold microdissection was performed via 355-nm laser ablation (1-kHz repetition rate, max 42-µJ pulse power, and 1-ns pulse length) implemented through a Rapp OptoElectronic module that is scanner based coupled to the microscope. The Rapp module runs on the SysCon2 software (2.3.1), also coupled to the ZEN software through the Image Transfer function. For Ca^{2+} imaging, GCaMP6f and membrane marker (apical: claudinb:Lyn-GFP; basal: tp63:CAAX-GFP) signals were excited with 488 nm and collected via band pass (BP) 535/30. For Voltron2 imaging, Voltron2:JF552 signals were excited with 561 nm and collected via BP 629/62. Continuous imaging (100 ms per frame) in a single *z* plane was performed, while ablation was triggered at a prespecified time frame (with a long pass beamsplitter T387LP in place). The scanning speed and position of the ablation laser are kept invariant across embryos, such that the microdissection takes place at ~50 µm away from the tip of the finfold and the triggered ablation laser traverses the tissue in 100 ms. The ablation laser power was estimated and adjusted per embryo to minimize positional shifts and cavity bubbles (due to excessive heating) while generating a line wound.

While most UV-laser ablation experiments were performed using the continuous-imaging setting described above (Figs. 1 and 2; fig. S2, S4, S5, A and C, and S6; and movies S1, S5, S7, S8, and S9), the experiments in figs. S3 and S5B and movies S2 and S6 followed a UV-laser ablation regime where time-lapse imaging before and after laser ablation were executed as two separate experimental blocks. In this setting, the first frame of the second continuous imaging block (130 ms per frame) was taken as 0 s.

For Voltron2 measurements while applying high KCl, continuous imaging (3 s per frame) in a single *z* plane was performed, as KCl was pipetted at a prespecified time frame. Apical epithelial membranes (claudinb:Lyn-GFP, 488-nm excitation, and BP 535/30) and Voltron2:JF552 (561-nm excitation and BP 629/62) signals were taken sequentially during the time series. Live imaging was repeated at least five times with different biological replicates per condition and zebrafish line.

Embryo heat shocks

Heat shocks were performed at 37°C for 1 hour in a water bath, where up to 100 embryos were placed into a petri dish containing 30 ml of E3. For VSP overexpression experiments with *Tg(Hsp70:CiDr-VSP-L223f-mCherry^{cbg23Tg}) (VSP-OE)* and *Tg(Hsp70:CiDr-VSP-wt-mCherry^{cbg24Tg};tpte$^{-/-}$) (rescue)*, two heat shocks were performed: the first at 31 hours postfertilization, and the second at 42 hours postfertilization. Embryos were sorted for fluorescence and/or amputated after 6 hours from the last heat shock (48 hours postfertilization). Two to three independent experiments were performed, with different biological replicates per condition.

Mechanical amputations

Mechanical finfold amputations were performed at 48 hours postfertilization, as described previously (*72*, *75*). Before amputation, embryos were anesthetized with 0.1% Tricaine (MS-222, Sigma-Aldrich) dissolved in E3 medium.

Finfold regrowth assay

To study the effects of all perturbations (drugs, mutants, and overexpression) during regrowth after injury, finfolds were amputated with a 15-mm surgical razor blade (Braun) at a position posterior to the notochord. After, embryos were returned to E3 medium and incubated at 28.5°C until desired developmental stages, when they were further processed for live imaging, immunostaining, or proliferation assays. When live imaged, uncut and cut larvae were placed in a 96-well plate (CellView) in E3 with anesthetic and imaged in bright-field mode with an automated live cell confocal microscope CellVoyager CV7000 (Yokogawa) with a 4×/0.16 air objective at 2, 3 and 5 days postfertilization. Embryos were returned to E3 medium without anesthetic at the end of each imaging session. Two or three independent experiments were performed, with different biological replicates per condition.

Stereoscope Ca^{2+} imaging following finfold injury

To live capture Ca^{2+} signals following mechanically induced injuries, anesthetized fish were placed in a plastic petri dish (Greiner Bio-One), and finfolds were wounded with a handheld plastic pipette. Videos were taken with an iPhone 13 connected to the eyepiece of a stereoscope (Olympus SZX2 with a X-Cite Series 120PC Q LED lamp, ET 510 bandpass) by a smartphone adapter (Dörr SA-1).

Proliferation assay

To label proliferating cells, the EdU Click-iT Alexa Fluor 647 fluorophore kit (Thermo Fisher Scientific, #C10340) was used. Briefly,

larvae from different developmental or amputation time points were incubated at 4°C in E3 medium with 500 μM EdU in 10% DMSO for 1 hour. Embryos were then washed three times with E3 and fixed overnight in 4% paraformaldehyde at 4°C. After whole-mount immunostaining with anti-p63 to label basal epithelial cells, EdU detection was performed as per the manufacturer's protocol. Embryos were stored in 80% glycerol and 2% DABCO (Sigma-Aldrich) at 4°C, protected from light until imaging.

Immunofluorescence

Whole-mount immunostainings were performed as previously described (*72*). The primary antibodies used were rabbit anti-p63 (1:200; Abcam, #ab97865), mouse anti-VSP (1:100; BIOZOL, #75-485), rabbit anti-mCherry living colors (Clontech, #632496), mouse anti-ZO-1 (Thermo Fisher Scientific, #339100), mouse anti-E-cadherin (BD Bioscience, #610181), and rabbit anti-Cx43 (Cell Signaling, #3512S). The secondary antibodies used were Alexa Fluor 488 goat anti-rabbit (Life Technologies, #A11034), Alexa Fluor 488 goat anti-mouse IgG2a (immunoglobulin G 2a; Thermo Fisher Scientific, #A21131), Alexa Fluor 488 goat anti-mouse (Life Technologies, #A11001), Alexa Fluor 594 goat anti-mouse IgG2a (Thermo Fisher Scientific, #A21135) (all used at 1:500 dilution). 4′,6-diamidino-2-phenylindole (DAPI; #D9564, Sigma-Aldrich) was incubated with the secondary antibodies at 1:1000 dilution. Immunostainings were repeated at least two times with different biological replicates per marker and condition. Embryos were mounted for imaging in 0.5% low-melting agarose (Sigma-Aldrich, A9414) diluted in E3 or 80% glycerol and 2% DABCO (Sigma-Aldrich) diluted in phosphate-buffered saline.

Images were acquired with an inverted Zeiss LSM 880 AiryScan point-laser scanning confocal microscope equipped with a C-Apochromat 40×/1.2 water immersion objective (Zeiss) or a Zeiss Cell Discoverer with a Plan-Apochromat 50×/1.2 water immersion objective (Zeiss). For imaging connexin43 stainings, we used a Zeiss Lattice Lightsheet 7 equipped with a 13.3×/0.4 water immersion illumination objective and a 44.83×/1.0 water immersion detection objective, allowing isometric voxel resolution. Images were acquired using the software ZEN Blue (v3.10.103) for the light sheet and software ZEN 2011 Black edition and ZEN Blue v. 3.6.095.09000 for laser scanning confocal systems. Two or three independent experiments with different biological replicates were performed per marker and condition.

Transmission electron microscopy

Two-days postfertilization WT AB larvae were fixed in 2% paraformaldehyde, 2% glutaraldehyde, and 50 mM Hepes (pH 7.2) at room temperature for 1 hour and then transferred to 4°C overnight. Then, the fixative was washed 3 × 5 min with 50 mM Hepes and rinsed with water before contrasting with reduced osmium tetroxide [1% OsO_4 (Electron Microscopy Sciences, EMS) and 1.5% K^+ ferrocyanide (Sigma-Aldrich)] in water for 1 hour at room temperature. Samples were then washed at least three times with ultrapure water between each staining and contrasting step. Staining was enhanced by incubation with 0.2% tannic acid (EMS) for 15 min at room temperature. A further contrasting step with 0.5% uranyl acetate (EMS) in water followed for 1 hour at room temperature in the dark. The tissue was further washed with water and then gradually dehydrated with increasing concentrations of ethanol (starting at 30% ethanol and finishing with 3× 100% ethanol incubation for 15, 15, and 30 min), followed by a stepwise infiltration with epoxy resin:ethanol (1:2, 1:1, and 2:1; EMBed 812, EMS). A final infiltration step in pure resin was performed at least overnight. The resin was lastly cured at 60°C for at least 24 hours. For conventional transmission electron microscopy analysis, 70-nm sections were cut on a Leica UCT ultramicrotome (Leica Microsystems, Wetzlar, Germany) onto formvar-coated slot grids and post stained with 2% aqueous uranyl acetate and lead citrate (EMS). Sections were collected at the notochord level (~160 μm from finfold tip; fig. S1C) and at 35 μm from the finfold tip (Fig. 1B). Images were taken on a Tecnai BioTwin T12 electron microscope (Philips/Thermo Fisher Scientific) with a F416 charge-coupled device camera (Tietz Video and Image Processing Systems). Two independent experiments were performed with at least four biological replicates each.

Statistical analysis

Movie registration

To correct for tissue displacement resulting from UV-laser cut and subsequent tissue contraction, raw image stacks collected from ZEN Blue software were imported to ImageJ (v2.14.0) and processed via the "bUnwrapJ" (v2.6.13) plugin (*106*). Specifically, the UV-laser cut was taken as a boundary condition that separates the tissue into two subimages, and a B-spline representation was used to elastically align each subimage to the image before cut (fig. S14, A and B). The two aligned subimages were then combined at the cut site (Fig. 1H and fig. S4, A to D).

This registration was performed for Voltron2 images (up to 5 s after cut) but not GCaMP6f images (up to 45 s after cut), as prominent injury-induced tissue contraction at >10 s after cut renders the alignment less accurate. For the KCl supplement experiments (fig. S6E and S15), this registration was performed for both Voltron2 and membrane marker images (GFP labeled), as tissue displacements due to imaging drifts (up to 5 min) are less prominent. See also fig. S14.

Epithelial cell segmentation and registration

To obtain segmentation of individual epithelial cells, registered image stacks were processed via the "cyto" model in Cellpose (v2.2.3, autocalibrated cell diameter per image stack) (*107*). Segmented masks from Cellpose were then imported to custom MATLAB (R2022b) scripts for following single-cell registration and analyses. Two different cell registration strategies were used. For apical epithelia, GCaMP6f signals were measured for up to 45 s after microdissection. We registered a list of moving cell positions by first segmenting the double transgenics (ubb:GCaMP6f;claudinb:Lyn-GFP) at every time frame and then tracking the center of mass across all time frames (Hungarian-based particle linker (*108*), distance cutoff for frame-to-frame linking set to 10 pixels = 2.76 μm, and no particle disappearance gap allowed). A round of manual correction was then performed (custom MATLAB script) to validate the tracked cells and remove artifacts. For basal epithelia, GCaMP6f signals were measured using a list of static cell positions because of the limited accuracy of Cellpose's cyto model in segmenting double transgenics ubb:GCaMP6f;-tp63:CAAX-GFP, in particular when GCaMP6f has a high cytosolic intensity. In this case, we measured single-cell GCaMP6f intensities for up to 10 s after UV-laser microdissection (fig. S2D). We also performed cell-independent wavefront evaluation of GCaMP6f change of intensity to ensure a reliable comparison with apical GCamp6f signals (fig. S2B). For apical and basal Voltron2:JF552 signals, measured for up to 5 s after UV-laser microdissection, we registered a list of static cell positions by segmenting the uncut or

untreated membrane reference image (see section "Voltron2:JF552 membrane signal quantification") in uncut finfolds, 100 ms before UV-laser microdissection was applied. In this case, a round of manual correction was performed in the graphical user interface (GUI) of Cellpose to remove artifacts.

GCaMP6f cytosolic signal quantification

To quantify GCaMP6f dynamics in individual cells from epithelial layer–specific datasets, we performed the signal quantification using double transgenics labeling both cytosolic Ca^{2+} (ubb:GCaMP6f) and one of the following membrane markers: claudinb:Lyn-GFP or tp63:CAAX-GFP. We verified that the change of intensity in the double transgenics comes from the change in cytosolic Ca^{2+} instead of the membranes labeled by GFP by comparing the postinjury signals in transgenics expressing only cytosolic Ca^{2+} or the membrane marker - see movies S10 and S11 and compare to movie S1. Only cytosolic signals were extracted from the double transgenic datasets (see segmentation above), avoiding membrane GFP signals from the epithelial membrane reporter transgenics. This was done by first registering a list of cell mass centers and boundaries via segmentation (see the section before). For each cell, the cytosolic GCaMP6f intensity was then extracted as the mean intensity of pixels enclosed by a proportionally contracted cell boundary (80% the distance to the center of mass r_c compared to the segmented boundary r_s, $r_{cyto} = 0.8 \times (r_s - r_c) + r_c$. To compare Ca^{2+} activation dynamics across embryos that could have different GCaMP6f insertion sites, the cellular change of GCaMP6f intensity (as compared to the GCaMP6f intensity before laser microdissection, $\Delta F = F - F_{uncut}$; here, F_{uncut} is the GCaMP6f average intensity across 3 s before cut) was first normalized by the maximum intensity change across all cells ($_{max}\Delta F$), a quantity specific to each embryo. The single-cell Ca^{2+} activation time was then determined by evaluating the time when this normalized cellular change of GCaMP6f intensity ($\Delta F/_{max}\Delta F$) surpasses a threshold (fixed to 0.1 throughout all analyses) for the first time. On the basis of the subsecond sharp increase of GCaMP6f intensity for cells close to the cut (Fig. 2C), we also performed a 10-point linear interpolation (10 ms per interpolated time point, compared to raw intensity time lapse at 100 ms per frame) between consecutive time points to extract an accurate estimate of when $\Delta F/_{max}\Delta F$ surpasses 0.1. Fitting the single-cell distance from cut (defined as its mass center from the line instructed for UV-laser microdissection) as a function of the activation time (nonlinear least square method, MATLAB) then returns the fitted Ca^{2+} wavefront activation dynamics (Fig. 1F). In *kcnh2a*$^{lof/lof}$ and FK506-treated embryos, a prominent fraction of cells spatially disconnected from the Ca^{2+} wavefront showed rapid Ca^{2+} activation within the initial seconds postinjury (i.e., Ca^{2+} flashes; Fig. 2, I and J), possibly resulting from increased expression of *kcnh2a* (*51*) or increased K^+ leak through *kcnk5b* (*47*, *49*, *54*) in the epithelium. These cells were excluded (manual filter, custom MATLAB script) in fitting of the Ca^{2+} wavefront dynamics (Fig. 2J and fig. S7B). On the other hand, Ca^{2+} flashes were determined by detecting local peaks ("islocalmax" function; MATLAB) in the normalized single-cell change of GCaMP6f intensity ($\Delta F/_{max}\Delta F$) that is not identified to be a first-time Ca^{2+} wavefront activation from above. A threshold of prominence (defined as the maximum height this local peak displays relative to neighboring valleys, threshold fixed to 0.15 throughout all analyses) was used to keep only those prominent local peaks. The detected peaks were lastly passed through a round of manual proofread to ensure the absence of artifacts (Figs. 1F and 2, I and K).

In addition to layer-specific single-cell GCaMP6f quantification, an additional quantification pipeline was developed to evaluate GCaMP6f intensity changes in datasets without epithelial membrane markers. This was performed for ubb:GGCaMP6f in the background of *tpte*$^{-/-}$ (in comparison to WT; fig. S12H). In this pipeline, GCaMP6f pixel intensity changes (ΔF) were also normalized by the maximum intensity change of all pixels ($_{max}\Delta F$) for each embryo. Instead of evaluating the activation time per single cell, pixels enclosed by the boundary of the caudal finfold (the boundary was created manually and excludes evident fibroblasts or notochord composition) were binned (20-μm width, based on segmented cell size; fig. S8G) according to their distances from cut, and activation time was defined as when the average normalized intensity change in a bin surpasses the same threshold [mean(ΔF)/$_{max}\Delta F > 0.1$] for the first time. The binned distance plotted versus the bin activation time then constitutes a simplified evaluation of the concomitant wavefront propagation dynamics for both apical and basal epithelial layers (fig. S12H). Last, for datasets with epithelial membrane markers, we also used the membrane marker–independent approach to evaluate the position and instantaneous velocity of the Ca^{2+} wavefront. This was done by plotting the normalized change of GCaMP6f intensity as a function of distance (no binning; distance is in unit of pixels) for every time frame and annotating the position where this normalized value drops to 0.1 as the instantaneous wavefront position (fig. S2B). Evaluating the instantaneous wavefront velocity (defined as the wavefront position after 1 s = 10 frames minus the current position) then determines the time when the wavefront velocity drops to 0 (Fig. 1D). This time (~5 s for both apical and basal layers) was thus used as the time range for fitting the Ca^{2+} wavefront activation dynamics. Custom MATLAB scripts are available at (*109*).

Voltron2:JF552 membrane signal quantification

To quantify single-cell membrane Voltron2:JF552 signals in an epithelial layer–specific manner (Voltron2 mRNA–injected into claudinb:Lyn-GFP or tp63:CAAX-GFP transgenics and then stained with JF552), we first obtained a list of static cell boundaries via segmentation of the membrane reference image (see the section "Epithelial cell segmentation and registration"). Here, because of the variability of Voltron2 expression and JF552 staining in the epithelial layers, the membrane reference image is either the uncut claudinb:Lyn-GFP or tp63:CAAX-GFP (when Voltron2:JF552 primarily appears at the epithelial layer labeled by transgenic membrane marker) or the uncut Voltron2:JF552 image (when Voltron2:JF552 primarily appears at the epithelial layer not labeled by transgenic membrane marker). In the latter case, we manually exclude cells whose membranes show both the transgenic and the Voltron2:JF552 signals (GUI of Cellpose) to ensure all registered cells come from the same epithelial layer. Next, these segmented cell boundaries were used to determine position of the membrane pixels. This was defined by extracting all pixels enclosed by a sliding square window with the radius of 3 pixels = 0.828 μm on the cell boundary (fig. S14, A and B). Here, the effective "membrane thickness" (6 pixels = 1.656 μm) was estimated by plotting the Tg(b-act:lyn-tdTomato) membrane marker (same imaging setup as Voltron2:JF552) intensity versus pixel distance from membrane and extracting the half-max width of the intensity distribution.

The change of Voltron2:JF552 intensities before and after cut was evaluated all for elastically registered images (see section "Movie registration" and compare fig. S14, C and D, for the improvement based on correcting tissue displacement). As a result, displacement-induced changes of Voltron2 intensity were minimized.

Changes of Voltron2:JF552 intensities [compared to the frame before cut, $\Delta F = F - F_{uncut}$; here, F_{uncut} is the Voltron2:JF552 average intensity at the time point right before cut (i.e., 0.1 s)] across all extracted membrane pixels were then binned according to their distance from cut (2-μm width) to evaluate the raw drop of membrane Voltron2:JF552 intensities in comparison to claudinb:Lyn-GFP or tp63:CAAX-GFP membrane marker controls (fig. S4E).

To obtain cell-averaged membrane signals, raw Voltron2:JF552 intensities from the membrane pixels from the boundary of the same cell were averaged. The resulting cellular Voltron2:JF552 time traces were then passed through a filter that excludes cells with a large fluctuation even before laser microdissection onsets (here taken as the range of cellular intensity is smaller than 10% of the mean of cellular intensity before cut) (Fig. 1I). The fractional drop of cell-averaged Voltron2:JF552 signals after laser microdissection ($-\Delta F/F_{uncut}$) was subsequently determined (Fig. 1, J and K). Noting that laser microdissection brings about a level of membrane intensity changes close to the cut site (Fig. 1H), we used a noise floor method to fit only the cells that exhibited Voltron2:JF552 signal changes that are above the membrane controls. The noise floor was constructed by binning the cell-averaged membrane signals according to their center-of-mass distance from cut (2-μm width) for the microdissected membrane controls (fig. S4F, left). Then, only Voltron2:JF552 cells within this binned distance that exhibited a bigger change compared to this noise floor were kept (fig. S4F, right). The fractional drops of these Voltron2:JF552 cells were then fitted as a simple exponential function of single-cell distance from cut (nonlinear least square method; MATLAB). The rationale for choosing an exponential fit followed that without a priori knowledge this is the simplest function that displays a decay over a (single) characteristic length scale. To capture the length of the depolarization gradient, we fitted this function with cells that are in the range of 30 to 150 μm from the cut site; cells within the first 0 to 30 μm are immediately adjacent to the cut site damaged by the UV laser (average cell area in fig. S8G), hence were discarded from our analyses. From 150 μm onward, different finfold samples contribute unevenly to the statistics, as small differences in the flatness of mounted samples result in these cells to be out of the field of view (e.g., fig. S4A).

Note that for Voltron2 signal quantification in KCl-treated apical cells, perfusion of high-concentration KCl (see "Chemical treatments, High KCl supplement" section) induces finfold contraction, thus causing a small shift of the *z*-focus (fig. S15, A and B) that cannot be reliably reconstructed by simple image registration assuming in-plane deformation. To exclude this effect, we used dual-color channel imaging (see "Spinning disk live imaging and UV-laser microdissection" section) to capture both Voltron2 and respective membrane marker (transgenic: claudinb:Lyn-GFP) signals. The Voltron2 signal extracted per cell was first normalized by the membrane GFP signal per cell [$F = F$(Voltron2)/F(claudinb:Lyn-GFP); fig. S15C]. This normalized Voltron2 intensity F was then used to calculate the change of Voltron2 signal compared to untreated time point ($\Delta F = F - F_{untreated}$; fig. S15D) and the fractional drop of Voltron2 signal ($-\Delta F/F_{untreated}$; fig. S6E). Custom MATLAB scripts for all Voltron2:JF552 signal analyses are available at (*110*).

Caudal finfold and body length quantifications

Finfold (Fig. 3A) and body lengths were manually measured from acquired whole-body bright-field images with the line tool in ImageJ v. 1.54 f (*111*). Finfold length was measured from the end of the notochord to the tip of this organ (Fig. 3A), while body length was measured from the mouth to the tip of the caudal finfold, along the notochord. Data were plotted and statistically analyzed using GraphPad Prism v. 10.4.1 (see figure legends). Data were tested for normality (Gaussian distribution) using the Kolmogorov-Smirnov test. In case of a normal distribution, unpaired, parametric, two-tailed *t* tests were used. In case of nonnormal distribution, unpaired, nonparametric, two-tailed Mann-Whitney tests were used.

Finfold epithelial layer thickness and interstitial space quantification

Quantification of the thickness of the apical and basal finfold epithelia was performed on images acquired at the Zeiss Lattice Lightsheet 7, which allows for isotropic resolution in *XYZ*. Uncut caudal finfolds of fixed double transgenics (tp63:CAAX-GFP and b-act:lyn-tdTomato) embryos were imaged, and the cumulative thickness of apical and basal epithelial layers was measured with the Fiji line tool from *XZ* projections at different distances from the finfold tip (fig. S1, C and D).

For measurements of the finfold's interstitial space, concerning area to perimeter ratio, the area between the dorsal and ventral epithelial layers was traced from the same uncut finfolds using the polygon selection tool, and measurements of the area and perimeter were extracted. Measurements were performed at the usual injury position (50 μm from the tip) used for all experiments in Figs. 1 and 2 and at various distances from that position (fig. S1, C and E).

Proliferation quantification

Quantification of the proliferation patterns and levels was performed using z-stacks of larval finfolds encompassing the full organ volumes acquired at different time points. To quantify the percentage of proliferative cells over total cell number over time, Imaris v.10.1.1 spot detection was used to count EdU^+, $p63^+$, and $DAPI^+$ cells in uncut and cut finfolds of various developmental and regenerative times. A spot radius of 4 μm was used for DAPI, and 6 μm was used for EdU and p63. The Imaris machine learning algorithm was then used to differentiate nuclei in the finfold from nuclei in the notochord, which were then used to spatially align the finfolds but excluded from the analysis. To quantify the spatial distribution of proliferative cells in larval finfolds, the *XY* coordinates of each detected spot were extracted from Imaris. A custom made Python3 script (v 0.0.1) (*112*) was generated to plot the ratio of proliferative cells (EdU^+) over total cells according to their position in the finfold, as a kernel density estimation. To align all finfolds, first, the quantiles of the distribution of *XY* position of all spots were computed and used to reorient all finfolds with the cut or tip of the finfold to the right. Then, the principal components analysis of the *XY* positions of cells in the notochord was computed, and the first component was taken to align the notochord horizontally. Bins of 20 μm were used when computing the EdU/DAPI ratio, as the average cell diameter of 48-hours postfertilization finfold epithelial cells is 18 μm (fig. S8G). To obtain heatmaps of the spatial distribution of proliferative cells, the finfolds from each group were first aligned and centered with respect to the tip of the notochord, and their datasets were merged. Then, the pixel of unit value representing the centroid of the cell (obtained from the Imaris spot detection) was plotted, and a Gaussian blur of 10 μm (sigma, corresponding to the cell radius) was applied to each spot to simulate a point spread function. Last, the values were normalized by the sum of the image matrix to obtain a position probability density. The values of the density were then mapped to a color map upon plotting. To keep good resolution in the finfold and avoid cells in the notochord, the value of density was kept in a

range between zero and a common clipping value of the color map. Three independent experiments were performed per condition. Statistical experimental details can be found in respective figure legends.

VSP intensity quantification

To quantify the expression of VSP in WT, *tpte*$^{-/-}$, and VSP-OE, a square region of interest of 96.93 μm^2 was drawn between the end of the notochord and the finfold tip, and mean fluorescence intensity was measured in Fiji. All values of intensity were then normalized to the average intensity of VSP staining in WT. Experiments were repeated at least two times with different biological replicates per condition. Data were plotted and statistically analyzed in GraphPad Prism 10.4.1. Statistical experimental details can be found in respective figure legends.

Estimation of proliferation contribution to finfold area

To estimate how cell proliferation 1 to 3 hours postdamage is essential for recovery of organ morphology, we considered the length and width of the finfold at 3 days postamputation for WT and *tpte*$^{-/-}$. We approximated the finfold as a semiellipse (fig. S12L) to obtain total areas (fig. S12O) from fin length (Fig. 4J) and width (fig. S12N) and calculated the difference between WT and *tpte*$^{-/-}$, corresponding to the missing regenerated area (fig. S12L). Furthermore, we used the average cell area (fig. S8G), the total number of cells in the finfold (fig. S12M), the percentage of proliferating cells at 1 and 3 hours postamputation (Fig. 3C), and the distribution of proliferation among layers (Fig. 4B) to calculate the contribution of proliferation to finfold area (fig. S12O). Specifically:

Finfold area contribution of 1-hours postamputation cell proliferation per single layer:

1300 cells × 10/100 = 130 × 250 μm^2 = 32,500 μm^2/2 layers = 16,250 μm^2

Finfold area contribution of 3-hours postamputation cell proliferation per single layer:

1300 cells × 8/100 = 104 × 250 μm^2 = 26,000 μm^2/2 layers = 13,000 μm^2

Finfold area contribution from 1- to 3-hours postamputation proliferation per single layer = 29,250 μm^2

Supplementary Materials

The PDF file includes:

Supplementary Theory Notes S1 to S6
Figs. S1 to S20
Legends for movies S1 to S11
References

Other Supplementary Material for this manuscript includes the following:

Movies S1 to S11

REFERENCES

1. J. R. Lazzari-Dean, A. M. M. Gest, E. W. Miller, Measuring absolute membrane potential across space and time. *Annu. Rev. Biophys.* **50**, 447–468 (2021).
2. C. D. McCaig, A. M. Rajnicek, B. Song, M. Zhao, Controlling cell behavior electrically: Current views and future potential. *Physiol. Rev.* **85**, 943–978 (2005).
3. R. O. Becker, Stimulation of partial limb regeneration in rats. *Nature* **235**, 109–111 (1972).
4. R. B. Borgens, J. W. Vanable Jr., L. F. Jaffe, Bioelectricity and regeneration. I. Initiation of frog limb regeneration by minute currents. *J. Exp. Zool.* **200**, 403–416 (1977).
5. R. B. Borgens, J. W. Vanable Jr., L. F. Jaffe, Bioelectricity and regeneration: Large currents leave the stumps of regenerating newt limbs. *Proc. Natl. Acad. Sci. U.S.A.* **74**, 4528–4532 (1977).
6. D. S. Adams, A. Masi, M. Levin, H$^+$ pump-dependent changes in membrane voltage are an early mechanism necessary and sufficient to induce *Xenopus* tail regeneration. *Development* **134**, 1323–1335 (2007).
7. K. B. Hotary, K. R. Robinson, Endogenous electrical currents and voltage gradients in *Xenopus* embryos and the consequences of their disruption. *Dev. Biol.* **166**, 789–800 (1994).
8. F. Ferreira, S. Moreira, M. Zhao, E. H. Barriga, Stretch-induced endogenous electric fields drive directed collective cell migration in vivo. *Nat. Mater.* **24**, 462–470 (2025).
9. E. Braun, H. Ori, Electric-induced reversal of morphogenesis in *Hydra*. *Biophys. J.* **117**, 1514–1523 (2019).
10. A. T. Barker, L. F. Jaffe, J. W. Vanable, The glabrous epidermis of cavies contains a powerful battery. *Am. J. Physiol.* **242**, R358–R366 (1982).
11. T. B. Saw, X. Gao, M. Li, J. He, A. P. Le, S. Marsh, K.-h. Lin, A. Ludwig, J. Prost, C. T. Lim, Transepithelial potential difference governs epithelial homeostasis by electromechanics. *Nat. Phys.* **18**, 1122–1128 (2022).
12. S. D. Klyce, Electrical profiles in the corneal epithelium. *J. Physiol.* **226**, 407–429 (1972).
13. R. P. Gallemore, B. A. Hughes, S. S. Miller, Retinal pigment epithelial transport mechanisms and their contributions to the electroretinogram. *Prog. Retin. Eye Res.* **16**, 509–566 (1997).
14. H. H. Ussing, Transport of ions across cellular membranes. *Physiol. Rev.* **29**, 127–155 (1949).
15. J. Fadjukov, S. Wienbar, S. Hakanen, V. Aho, M. Vihinen-Ranta, T. O. Ihalainen, G. W. Schwartz, S. Nymark, Gap junctions and connexin hemichannels both contribute to the electrical properties of retinal pigment epithelium. *J. Gen. Physiol.* **154**, e202112916 (2022).
16. A. E. Pereda, S. Curti, G. Hoge, R. Cachope, C. E. Flores, J. E. Rash, Gap junction-mediated electrical transmission: Regulatory mechanisms and plasticity. *Biochim. Biophys. Acta* **1828**, 134–146 (2013).
17. C. Zihni, C. Mills, K. Matter, M. S. Balda, Tight junctions: From simple barriers to multifunctional molecular gates. *Nat. Rev. Mol. Cell Biol.* **17**, 564–580 (2016).
18. A. Torres-Sánchez, M. Kerr Winter, G. Salbreux, Tissue hydraulics: Physics of lumen formation and interaction. *Cell Dev.* **168**, 203724 (2021).
19. V. W. Tang, D. A. Goodenough, Paracellular ion channel at the tight junction. *Biophys. J.* **84**, 1660–1673 (2003).
20. D. M. Maurice, Epithelial potential of the cornea. *Exp. Eye Res.* **6**, 138–140 (1967).
21. B. Reid, B. Song, C. D. McCaig, M. Zhao, Wound healing in rat cornea: The role of electric currents. *FASEB J.* **19**, 379–386 (2005).
22. B. Reid, M. Zhao, The electrical response to injury: Molecular mechanisms and wound healing. *Adv. Wound Care* **3**, 184–201 (2014).
23. B. Reid, B. Song, M. Zhao, Electric currents in *Xenopus* tadpole tail regeneration. *Dev. Biol.* **335**, 198–207 (2009).
24. R. Nuccitelli, P. Nuccitelli, C. Li, S. Narsing, D. M. Pariser, K. Lui, The electric field near human skin wounds declines with age and provides a noninvasive indicator of wound healing. *Wound Repair Regen.* **19**, 645–655 (2011).
25. J. Monteiro, R. Aires, J. D. Becker, A. Jacinto, A. C. Certal, J. Rodríguez-León, V-ATPase proton pumping activity is required for adult zebrafish appendage regeneration. *PLOS ONE* **9**, e92594 (2014).
26. M. Chiang, K. R. Robinson, J. W. Vanable Jr., Electrical fields in the vicinity of epithelial wounds in the isolated bovine eye. *Exp. Eye Res.* **54**, 999–1003 (1992).
27. B. Reid, R. Nuccitelli, M. Zhao, Non-invasive measurement of bioelectric currents with a vibrating probe. *Nat. Protoc.* **2**, 661–669 (2007).
28. M. Chiang, E. J. Cragoe, J. W. Vanable, Intrinsic electric fields promote epithelization of wounds in the newt, *Notophthalmus viridescens*. *Dev. Biol.* **146**, 377–385 (1991).
29. L. Li, W. Gu, J. Du, B. Reid, X. Deng, Z. Liu, Z. Zong, H. Wang, B. Yao, C. Yang, J. Yan, L. Zeng, L. Chalmers, M. Zhao, J. Jiang, Electric fields guide migration of epidermal stem cells and promote skin wound healing. *Wound Repair Regen.* **20**, 840–851 (2012).
30. A. S. Kennard, J. A. Theriot, Osmolarity-independent electrical cues guide rapid response to injury in zebrafish epidermis. *eLife* **9**, e62386 (2020).
31. C. M. Illingworth, A. T. Barker, Measurement of electrical currents emerging during the regeneration of amputated finger tips in children. *Clin. Phys. Physiol. Meas.* **1**, 87 (1980).
32. J. V. Cordeiro, A. Jacinto, The role of transcription-independent damage signals in the initiation of epithelial wound healing. *Nat. Rev. Mol. Cell Biol.* **14**, 249–262 (2013).
33. S. K. Yoo, C. M. Freisinger, D. C. Lebert, A. Huttenlocher, Early redox, Src family kinase, and calcium signaling integrate wound responses and tissue regeneration in zebrafish. *J. Cell Biol.* **199**, 225–234 (2012).
34. M. Antunes, T. Pereira, J. V. Cordeiro, L. Almeida, A. Jacinto, Coordinated waves of actomyosin flow and apical cell constriction immediately after wounding. *J. Cell Biol.* **202**, 365–379 (2013).
35. K. Watanabe, K. Hashimoto, K. Hasegawa, H. Shindo, Y. Tsuruda, K. Kupisz, M. Koselski, P. Wasko, K. Trebacz, K. Kuchitsu, Rapid propagation of Ca^{2+} waves and electrical signals in the liverwort *Marchantia polymorpha*. *Plant Cell Physiol.* **65**, 660–670 (2024).
36. S. Chifflet, C. Justet, J. A. Hernández, V. Nin, C. Escande, J. C. Benech, Early and late calcium waves during wound healing in corneal endothelial cells. *Wound Repair Regen.* **20**, 28–37 (2012).

37. S. Xu, A. D. Chisholm, A Gαq-Ca^{2+} signaling pathway promotes actin-mediated epidermal wound closure in *C. elegans*. *Curr. Biol.* **21**, 1960–1967 (2011).
38. H. A. Benink, W. M. Bement, Concentric zones of active RhoA and Cdc42 around single cell wounds. *J. Cell Biol.* **168**, 429–439 (2005).
39. J. Yin, K. Xu, J. Zhang, A. Kumar, F.-S. X. Yu, Wound-induced ATP release and EGF receptor activation in epithelial cells. *J. Cell Sci.* **120**, 815–825 (2007).
40. B. Enyedi, S. Kala, T. Nikolich-Zugich, P. Niethammer, Tissue damage detection by osmotic surveillance. *Nat. Cell Biol.* **15**, 1123–1130 (2013).
41. W. J. Gault, B. Enyedi, P. Niethammer, Osmotic surveillance mediates rapid wound closure through nucleotide release. *J. Cell Biol.* **207**, 767–782 (2014).
42. P. Niethammer, C. Grabher, A. T. Look, T. J. Mitchison, A tissue-scale gradient of hydrogen peroxide mediates rapid wound detection in zebrafish. *Nature* **459**, 996–999 (2009).
43. B. Enyedi, M. Jelcic, P. Niethammer, The cell nucleus serves as a mechanotransducer of tissue damage-induced inflammation. *Cell* **165**, 1160–1170 (2016).
44. J. L. Moore, D. Bhaskar, F. Gao, C. Matte-Martone, S. Du, E. Lathrop, S. Ganesan, L. Shao, R. Norris, N. Campamà Sanz, K. Annusver, M. Kasper, A. Cox, C. Hendry, B. Rieck, S. Krishnaswamy, V. Greco, Cell cycle controls long-range calcium signaling in the regenerating epidermis. *J. Cell Biol.* **222**, e202302095 (2023).
45. K. D. Poss, E. M. Tanaka, Hallmarks of regeneration. *Cell Stem Cell* **31**, 1244–1261 (2024).
46. A. D. Hoptak-Solga, K. A. Klein, A. M. DeRosa, T. W. White, M. K. Iovine, Zebrafish short fin mutations in connexin43 lead to aberrant gap junctional intercellular communication. *FEBS Lett.* **581**, 3297–3302 (2007).
47. S. Perathoner, J. M. Daane, U. Henrion, G. Seebohm, C. W. Higdon, S. L. Johnson, C. Nüsslein-Volhard, M. P. Harris, Bioelectric signaling regulates size in zebrafish fins. *PLOS Genet.* **10**, e1004080 (2014).
48. S. Kujawski, W. Lin, F. Kitte, M. Börmel, S. Fuchs, G. Arulmozhivarman, S. Vogt, D. Theil, Y. Zhang, C. L. Antos, Calcineurin regulates coordinated outgrowth of zebrafish regenerating fins. *Dev. Cell* **28**, 573–587 (2014).
49. J. M. Daane, J. Lanni, I. Rothenberg, G. Seebohm, C. W. Higdon, S. L. Johnson, M. P. Harris, Bioelectric-calcineurin signaling module regulates allometric growth and size of the zebrafish fin. *Sci. Rep.* **8**, 10391 (2018).
50. M. R. Silic et al., Potassium channel-associated bioelectricity of the dermomyotome determines fin patterning in zebrafish. *Genetics* **215**, 1067–1084 (2020).
51. S. Stewart, H. K. le Bleu, G. A. Yette, A. L. Henner, A. E. Robbins, J. A. Braunstein, K. Stankunas, *longfin* causes cis-ectopic expression of the *kcnh2a ether-a-go-go* K^+ channel to autonomously prolong fin outgrowth. *Development* **148**, dev199384 (2021).
52. J. M. Daane, N. Blum, J. Lanni, H. Boldt, M. K. Iovine, C. W. Higdon, S. L. Johnson, N. R. Lovejoy, M. P. Harris, Modulation of bioelectric cues in the evolution of flying fishes. *Curr. Biol.* **31**, 5052–5061.e8 (2021).
53. H. K. Le Bleu, R. G. Kioussi, A. L. Henner, V. M. Lewis, S. Stewart, K. Stankunas, Voltage-gated calcium channels generate blastema Ca^{2+} fluxes restraining zebrafish fin regenerative outgrowth. *Development* **152**, dev204739 (2025).
54. C. Yi, T. W. Spitters, E. A.-D. A. Al-Far, S. Wang, T. L. Xiong, S. Cai, X. Yan, K. Guan, M. Wagner, A. El-Armouche, C. L. Antos, A calcineurin-mediated scaling mechanism that controls a K^+–leak channel to regulate morphogen and growth factor transcription. *eLife* **10**, e60691 (2021).
55. R. W. M. Kwong, S. F. Perry, The tight junction protein claudin-b regulates epithelial permeability and sodium handling in larval zebrafish, *Danio rerio*. *Am. J. Physiol. Regul. Integr. Comp. Physiol.* **304**, R504–R513 (2013).
56. B. Belardi, T. Hamkins-Indik, A. R. Harris, J. Kim, K. Xu, D. A. Fletcher, A weak link with actin organizes tight junctions to control epithelial permeability. *Dev. Cell* **54**, 792–804.e7 (2020).
57. R. B. Bird, , W. E. Stewart, E. N. Lightfoot, *Transport Phenomena* (Wiley, 2007).
58. W. M. Haynes, *CRC Handbook of Chemistry and Physics* (CRC Press, 2016).
59. I. Semenov, S. Xiao, A. G. Pakhomov, Primary pathways of intracellular Ca^{2+} mobilization by nanosecond pulsed electric field. *Biochim. Biophys. Acta* **1828**, 981–989 (2013).
60. Q. Chen, J. Cichon, W. Wang, L. Qiu, S.-J. R. Lee, N. R. Campbell, N. Destefino, M. J. Goard, Z. Fu, R. Yasuda, L. L. Looger, B. R. Arenkiel, W.-B. Gan, G. Feng, Imaging neural activity using *Thy1*-GCaMP transgenic mice. *Neuron* **76**, 297–308 (2012).
61. A. S. Abdelfattah, J. Zheng, A. Singh, Y.-C. Huang, D. Reep, G. Tsegaye, A. Tsang, B. J. Arthur, M. Rehorova, C. V. L. Olson, Y. Shuai, L. Zhang, T.-M. Fu, D. E. Milkie, M. V. Moya, T. D. Weber, A. L. Lemire, C. A. Baker, N. Falco, Q. Zheng, J. B. Grimm, M. C. Yip, D. Walpita, M. Chase, L. Campagnola, G. J. Murphy, A. M. Wong, C. R. Forest, J. Mertz, M. N. Economo, G. C. Turner, M. Koyama, B.-J. Lin, E. Betzig, O. Novak, L. D. Lavis, K. Svoboda, W. Korff, T.-W. Chen, E. R. Schreiter, J. P. Hasseman, I. Kolb, Sensitivity optimization of a rhodopsin-based fluorescent voltage indicator. *Neuron* **111**, 1547–1563.e9 (2023).
62. S. F. G. Krens, J. H. Veldhuis, V. Barone, D. Čapek, J.-L. Maître, G. W. Brodland, C.-P. Heisenberg, Interstitial fluid osmolarity modulates the action of differential tissue surface tension in progenitor cell segregation during gastrulation. *Development* **144**, 1798–1806 (2017).
63. A. Vian, M. Pochitaloff, S.-T. Yen, S. Kim, J. Pollock, Y. Liu, E. M. Sletten, O. Campàs, In situ quantification of osmotic pressure within living embryonic tissues. *Nat. Commun.* **14**, 7023 (2023).
64. P. Dayan, L. F. Abbott, *Theoretical Neuroscience: Computational and Mathematical Modeling of Neural Systems* (Massachusetts Institute of Technology Press, 2001).
65. S. Brzychczy, R. R. Poznanski, *Mathematical Neuroscience* (Academic Press, 2014).
66. S. H. Wright, Generation of resting membrane potential. *Adv. Physiol. Educ.* **28**, 139–142 (2004).
67. M. Cameron, O. Kékesi, J. W. Morley, J. Tapson, P. P. Breen, A. van Schaik, Y. Buskila, Calcium imaging of AM dyes following prolonged incubation in acute neuronal tissue. *PLOS ONE* **11**, e0155468 (2016).
68. J. S. Lanni, D. Peal, L. Ekstrom, H. Chen, C. Stanclift, M. E. Bowen, A. Mercado, G. Gamba, K. T. Kahle, M. P. Harris, Integrated K^+ channel and K^+Cl^- cotransporter functions are required for the coordination of size and proportion during development. *Dev. Biol.* **456**, 164–178 (2019).
69. S. A. N. Goldstein, D. Bockenhauer, I. O'Kelly, N. Zilberberg, Potassium leak channels and the KCNK family of two-p-domain subunits. *Nat. Rev. Neurosci.* **2**, 175–184 (2001).
70. C. K. Bauer, J. R. Schwarz, Ether-à-go-go K^+ channels: Effective modulators of neuronal excitability. *J. Physiol.* **596**, 769–783 (2018).
71. M. J. Perrin, R. N. Subbiah, J. I. Vandenberg, A. P. Hill, Human ether-a-go-go related gene (hERG) K^+ channels: Function and dysfunction. *Prog. Biophys. Mol. Biol.* **98**, 137–148 (2008).
72. R. Mateus, T. Pereira, S. Sousa, J. E. de Lima, S. Pascoal, L. Saúde, A. Jacinto, In vivo cell and tissue dynamics underlying zebrafish fin fold regeneration. *PLOS ONE* **7**, e51766 (2012).
73. A. Nechiporuk, M. T. Keating, A proliferation gradient between proximal and msxb-expressing distal blastema directs zebrafish fin regeneration. *Development* **129**, 2607–2617 (2002).
74. M. Zhao, B. Song, J. Pu, T. Wada, B. Reid, G. Tai, F. Wang, A. Guo, P. Walczysko, Y. Gu, T. Sasaki, A. Suzuki, J. V. Forrester, H. R. Bourne, P. N. Devreotes, C. McCaig, J. M. Penninger, Electrical signals control wound healing through phosphatidylinositol-3-OH kinase-gamma and PTEN. *Nature* **442**, 457–460 (2006).
75. A. Kawakami, T. Fukazawa, H. Takeda, Early fin primordia of zebrafish larvae regenerate by a similar growth control mechanism with adult regeneration. *Dev. Dyn.* **231**, 693–699 (2004).
76. Y. Murata, H. Iwasaki, M. Sasaki, K. Inaba, Y. Okamura, Phosphoinositide phosphatase activity coupled to an intrinsic voltage sensor. *Nature* **435**, 1239–1243 (2005).
77. A. Ratanayotha, M. Matsuda, Y. Kimura, F. Takenaga, T. Mizuno, M. I. Hossain, S.-I. Higashijima, T. Kawai, M. Ogasawara, Y. Okamura, Voltage-sensing phosphatase (Vsp) regulates endocytosis-dependent nutrient absorption in chordate enterocytes. *Commun. Biol.* **5**, 948 (2022).
78. M. I. Hossain, H. Iwasaki, Y. Okochi, M. Chahine, S. Higashijima, K. Nagayama, Y. Okamura, Enzyme domain affects the movement of the voltage sensor in ascidian and zebrafish voltage-sensing phosphatases. *J. Biol. Chem.* **283**, 18248–18259 (2008).
79. Y. Murata, Y. Okamura, Depolarization activates the phosphoinositide phosphatase Ci-VSP, as detected in *Xenopus* oocytes coexpressing sensors of PIP2. *J. Physiol.* **583**, 875–889 (2007).
80. C. R. Halaszovich, D. N. Schreiber, D. Oliver, Ci-VSP is a depolarization-activated phosphatidylinositol-4,5-bisphosphate and phosphatidylinositol-3,4,5-trisphosphate 5'-phosphatase. *J. Biol. Chem.* **284**, 2106–2113 (2009).
81. A. Kawanabe, N. Mizutani, O. K. Polat, T. Yonezawa, T. Kawai, M. X. Mori, Y. Okamura, Engineering an enhanced voltage-sensing phosphatase. *J. Gen. Physiol.* **152**, e201912491 (2020).
82. Y. Zhou, C.-O. Wong, K.-j. Cho, D. van der Hoeven, H. Liang, D. P. Thakur, J. Luo, M. Babic, K. E. Zinsmaier, M. X. Zhu, H. Hu, K. Venkatachalam, J. F. Hancock, Membrane potential modulates plasma membrane phospholipid dynamics and K-Ras signaling. *Science* **349**, 873–876 (2015).
83. H. Lee, D. Kimelman, A dominant-negative form of p63 is required for epidermal proliferation in zebrafish. *dev. Cell* **2**, 607–616 (2002).
84. H. M. McNamara, R. Salegame, Z. A. Tanoury, H. Xu, S. Begum, G. Ortiz, O. Pourquie, A. E. Cohen, Bioelectrical domain walls in homogeneous tissues. *Nat. Phys.* **16**, 357–364 (2020).
85. J. Cervera, A. Pietak, M. Levin, S. Mafe, Bioelectrical coupling in multicellular domains regulated by gap junctions: A conceptual approach. *Bioelectrochemistry* **123**, 45–61 (2018).
86. Y. Okamura, A. Kawanabe, T. Kawai, Voltage-sensing phosphatases: Biophysics, physiology, and molecular engineering. *Physiol. Rev.* **98**, 2097–2131 (2018).
87. T. Ishida, T. Nakajima, A. Kudo, A. Kawakami, Phosphorylation of Junb family proteins by the Jun N-terminal kinase supports tissue regeneration in zebrafish. *Dev. Biol.* **340**, 468–479 (2010).
88. F. Knopf, C. Hammond, A. Chekuru, T. Kurth, S. Hans, C. W. Weber, G. Mahatma, S. Fisher, M. Brand, S. Schulte-Merker, G. Weidinger, Bone regenerates via dedifferentiation of osteoblasts in the zebrafish fin. *Dev. Cell* **20**, 713–724 (2011).
89. B. Z. Jia, Y. Qi, J. D. Wong-Campos, S. G. Megason, A. E. Cohen, A bioelectrical phase transition patterns the first vertebrate heartbeats. *Nature* **622**, 149–155 (2023).

90. G. Shim, I. B. Breinyn, A. Martínez-Calvo, S. Rao, D. J. Cohen, Bioelectric stimulation controls tissue shape and size. *Nat. Commun.* **15**, 2938 (2024).
91. M. Westerfield, *The Zebrafish Book; A Guide for the Laboratory Use of Zebrafish (Danio Rerio)* (University of Oregon Press, 2007).
92. F. J. M. van Eeden, M. Granato, U. Schach, M. Brand, M. Furutani-Seiki, P. Haffter, M. Hammerschmidt, C. P. Heisenberg, Y. J. Jiang, D. A. Kane, R. N. Kelsh, M. C. Mullins, J. Odenthal, R. M. Warga, C. Nüsslein-Volhard, Genetic analysis of fin formation in the zebrafish, *Danio rerio*. *Development* **123**, 255–262 (1996).
93. P. Haas, D. Gilmour, Chemokine signaling mediates self-organizing tissue migration in the zebrafish lateral line. *Dev. Cell* **10**, 673–680 (2006).
94. T. S. Lisse, L. J. Elias, A. D. Pellegrini, P. B. Martin, E. L. Spaulding, O. Lopes, E. A. Brochu, E. V. Carter, A. Waldron, S. Rieger, Paclitaxel-induced epithelial damage and ectopic MMP-13 expression promotes neurotoxicity in zebrafish. *Proc. Natl. Acad. Sci. U.S.A.* **113**, E2189–E2198 (2016).
95. P. Eckert, M. D. Knickmeyer, L. Schütz, J. Wittbrodt, S. Heermann, Morphogenesis and axis specification occur in parallel during optic cup and optic fissure formation, differentially modulated by BMP and Wnt. *Open Biol.* **9**, 180179 (2019).
96. F. Kroll, G. T. Powell, M. Ghosh, G. Gestri, P. Antinucci, T. J. Hearn, H. Tunbak, S. Lim, H. W. Dennis, J. M. Fernandez, D. Whitmore, E. Dreosti, S. W. Wilson, E. J. Hoffman, J. Rihel, A simple and effective F0 knockout method for rapid screening of behaviour and other complex phenotypes. *eLife* **10**, e59683 (2021).
97. J. L. Hartley, G. F. Temple, M. A. Brasch, DNA cloning using in vitro site-specific recombination. *Genome Res.* **10**, 1788–1795 (2000).
98. K. M. Kwan, E. Fujimoto, C. Grabher, B. D. Mangum, M. E. Hardy, D. S. Campbell, J. M. Parant, H. J. Yost, J. P. Kanki, C.-B. Chien, The Tol2kit: A multisite gateway-based construction kit for Tol2 transposon transgenesis constructs. *Dev. Dyn.* **236**, 3088–3099 (2007).
99. T.-W. Chen, T. J. Wardill, Y. Sun, S. R. Pulver, S. L. Renninger, A. Baohan, E. R. Schreiter, R. A. Kerr, M. B. Orger, V. Jayaraman, L. L. Looger, K. Svoboda, D. S. Kim, Ultrasensitive fluorescent proteins for imaging neuronal activity. *Nature* **499**, 295–300 (2013).
100. C. Mosimann, C. K. Kaufman, P. Li, E. K. Pugach, O. J. Tamplin, L. I. Zon, Ubiquitous transgene expression and Cre-based recombination driven by the ubiquitin promoter in zebrafish. *Development* **138**, 169–177 (2011).
101. S. Bhattacharya, C. Hyland, M. M. Falk, M. K. Iovine, Connexin 43 gap junctional intercellular communication inhibits evx1 expression and joint formation in regenerating fins. *Development* **147**, dev190512 (2020).
102. J. Konantz, C. L. Antos, Reverse genetic morpholino approach using cardiac ventricular injection to transfect multiple difficult-to-target tissues in the zebrafish larva. *J. Vis. Exp.*, e51595 (2014).
103. R. F. Fallon, D. A. Goodenough, Five-hour half-life of mouse liver gap-junction protein. *J. Cell Biol.* **90**, 521–526 (1981).
104. C. Hyland, M. Mfarej, G. Hiotis, S. Lancaster, N. Novak, M. K. Iovine, M. M. Falk, Impaired Cx43 gap junction endocytosis causes morphological and functional defects in zebrafish. *Mol. Biol. Cell* **32**, ar13 (2021).
105. Y. Li, C. Liu, X. Bai, M. Li, C. Duan, FK506-binding protein 5 regulates cell quiescence-proliferation decision in zebrafish epithelium. *FEBS Lett.* **597**, 1868–1879 (2023).
106. I. Arganda-Carreras, C. O. S. Sorzano, R. Marabini, J. M. Carazo, C. Ortiz-de-Solorzano, J. Kybic, "Consistent and elastic registration of histological sections using vector-spline regularization," in *Computer Vision Approaches to Medical Image Analysis*, R. R. Beichel, M. Sonka, Eds. (Springer, 2006), pp. 85–95.
107. M. Pachitariu, C. Stringer, Cellpose 2.0: How to train your own model. *Nat. Methods* **19**, 1634–1641 (2022).
108. J. Y. Tinevez, Simpletracker (GitHub, 2025).
109. J. Liu, Fast calcium signals upon fin injury analysis codes (Zenodo, 2025).
110. J. Liu, Membrane potential reporter analysis upon fin injury or KCl perfusion (Zenodo, 2025).
111. J. Schindelin, I. Arganda-Carreras, E. Frise, V. Kaynig, M. Longair, T. Pietzsch, S. Preibisch, C. Rueden, S. Saalfeld, B. Schmid, J.-Y. Tinevez, D. J. White, V. Hartenstein, K. Eliceiri, P. Tomancak, A. Cardona, Fiji: An open-source platform for biological-image analysis. *Nat. Methods* **9**, 676–682 (2012).
112. E. Nerli, Proliferation analysis fin (Zenodo, 2025); DOI: 10.5281/zenodo.15019089.
113. Y. Mori, From three-dimensional electrophysiology to the cable model: An asymptotic study. arXiv:0901.3914 [q-bio.NC] (2009).
114. C. Koch, *Biophysics of Computation: Information Processing in Single Neurons* (Oxford University Press, 2004).

Acknowledgments: We thank S. Grill, J. Brugués, A. Grapin-Botton, M. Huch, J. Rodenfels, and M. Marass for critical manuscript feedback. We thank L. D. Lavis for providing JF552-Halotag dye, P. Trus for initial efforts with Ca^{2+} live imaging in zebrafish, T. Bianucci and L. Ribas for help with the proliferation analysis pipeline, and F. Gawlas and P. Rustler for help with generating Ca^{2+} transgenic lines at the University of Freiburg. We are grateful to the following MPI-CBG facilities: Light Microscopy, Technology Development Studio, Electron Microscopy, Transgenic Core, and Zebrafish Unit. **Funding:** This work was supported by the Max Planck Society (to E.N., J.L., N.B., S.K., C.P., A.S.V., F.J., and R.M.) and the Deutsche Forschungsgemeinschaft (DFG; German Research Foundation) under Germany's Excellence Strategy - EXC-2068-390729961 - Cluster of Excellence Physics of Life of TU Dresden (to E.N., J.L., N.B., S.K., C.P., and R.M.). J.L. has also been supported by the ELBE Postdoctoral Fellowships Program. A.B.A. acknowledges support by the Baden-Württemberg Stiftung (Elite programme for Postdocs) and DFG grant EXC294 (BIOSS Centre for Biological Signalling Studies) while supported by W. Driever. **Author contributions:** Conceptualization: R.M., F.J., C.P., E.N., A.S.V., C.D., and J.L. Investigation: F.J., C.P., E.N., C.D., and J.L. Data curation: R.M., E.N., C.D., and J.L. Validation: C.P., E.N., C.D., and J.L. Formal analysis: F.J., C.P., E.N., A.S.V., C.D., and J.L. Methodology: R.M., N.B., F.J., E.N., A.B.A., A.S.V., C.D., S.K., and J.L. Resources: R.M., N.B., E.N., A.B.A., S.K., and J.L. Software: C.P., E.N., A.S.V., C.D., and J.L. Visualization: R.M., F.J., C.P., E.N., C.D., and J.L. Writing—original draft: R.M., F.J., E.N., A.S.V., C.D., and J.L. Writing—review and editing: R.M., F.J., E.N., A.B.A., A.S.V., C.D., and J.L. Supervision: R.M., F.J., and E.N. Funding acquisition: R.M., F.J., and J.L. Project administration: R.M. and F.J. All authors read and approved the final version of the manuscript. **Competing interests:** The authors declare that they have no competing interests. **Data and materials availability:** All data and code needed to evaluate and reproduce the results in the paper are present in the paper and/or the Supplementary Materials. Source data for the paper and the Supplementary Materials are deposited on Edmond: doi.org/10.17617/3.6WBOSZ. Custom code for analysis pipelines and simulations are available on Zenodo (doi.org/10.5281/zenodo.15019089, doi.org/10.5281/zenodo.15038032, doi.org/10.5281/zenodo.15037932, and doi.org/10.5281/zenodo.17397026). Plasmids and zebrafish lines generated in this study are available upon request to R.M. (mateus@mpi-cbg.de).

Submitted 5 September 2025
Accepted 1 January 2026
Published 4 February 2026
10.1126/sciadv.aec0687

Science Advances

Injury-induced electrochemical coupling triggers organ growth

Jinghui Liu, Elisa Nerli, Charlie Duclut, Amit S. Vishen, Naomi Berbee, Sylvia Kaufmann, Cesar Ponce, Aristides B. Arrenberg, Frank Jülicher, and Rita Mateus

Sci. Adv. **12** (6), eaec0687. DOI: 10.1126/sciadv.aec0687

Science Advances (ISSN 2375-2548) is published by the American Association for the Advancement of Science. 1200 New York Avenue NW, Washington, DC 20005. The title *Science Advances* is a registered trademark of AAAS.